MSc Thesis – Master Earth Structure & Dynamics

Microstructural analysis of epidote-amphibolites and plate interface rheology in warm subduction zones

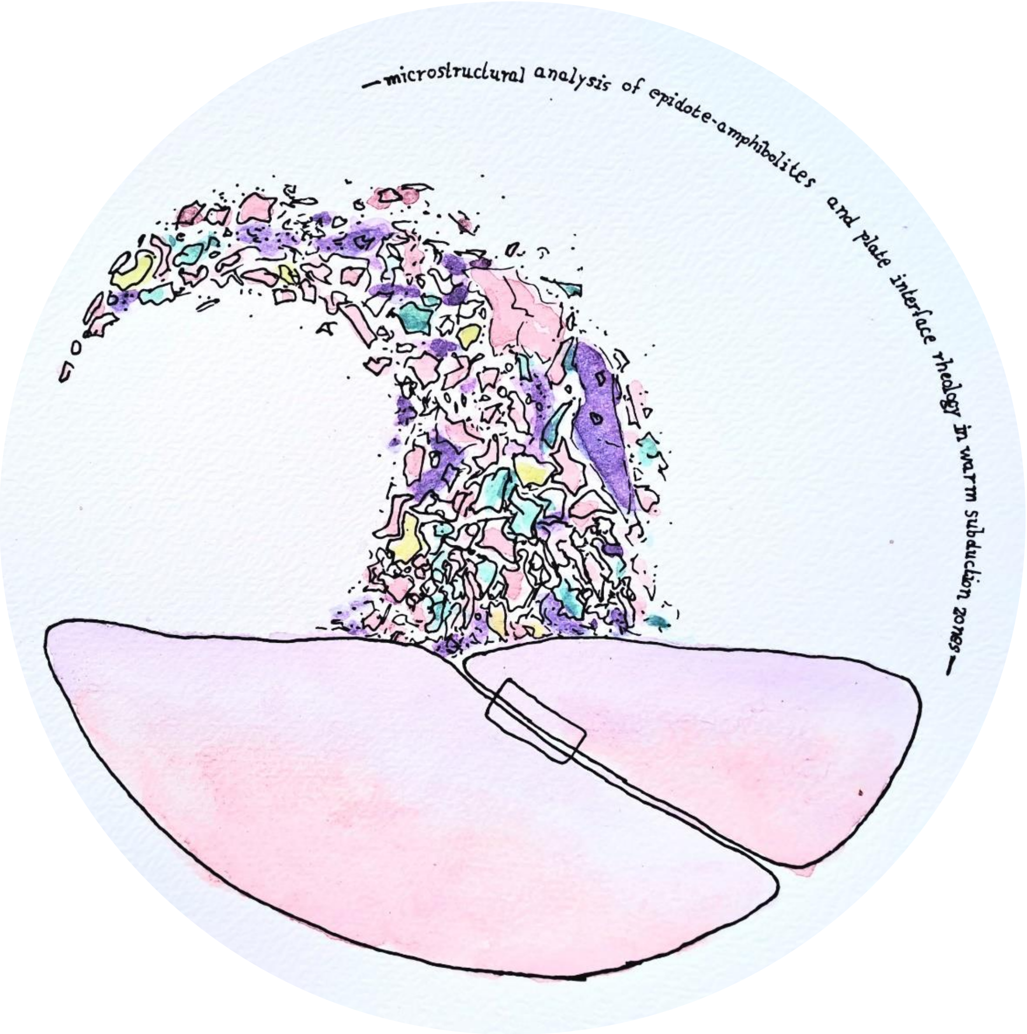

Laurens H. Kleijbeuker
Department of Earth Sciences, Utrecht University

April 29, 2024

Supervisor: Alissa J. Kotowski & Maartje F. Hamers

Acknowledgments

The author expresses heartfelt gratitude to Anneke Royakkers and Helene Kreuk for their unwavering support throughout the project. Their invaluable assistance was indispensable, and this thesis would not have reached completion without them.

Furthermore, the author wishes to extend enormous thanks to Alissa Kotowksi for her integral role in this captivating study. Gratitude is extended for sharing thin sections, entrusting the selection of areas for EBSD mapping, and for continuous feedback, guidance, and knowledge sharing throughout the project.

Special appreciation is also extended to Maartje Hamers for her thorough assistance during electron microscopy analyses, and to Hamed Amiri for sharing his code and his significant contributions to the connectivity analysis.

In addition, the author is grateful to Leo Kriegsman and Martyn Drury for their assistance during optical microscopy in mineral identification, Eric Hellebrand for aiding with the Syton polisher, Richard Wessels for capturing axioscan images, Hans de Bresser for sharing expertise on piezometry, and Alireza Chogani for initial support on connectivity.

The author acknowledges Andrew Keats for insightful and informal discussions on the project, Julius Pesola, Dominique Mes, and Silvi Klein-Schiphorst for their companionship during breaks, and Carla de Wolf for her assistance in reviewing this paper.

Lastly, the author thanks Jolinde Hooglander for drawing the art on the frontpage figure.

Abstract

A primary factor driving tectonic plate movement is the subduction of oceanic plates into the lithosphere. To initiate a subduction zone, a shear zone between the descending oceanic crust and overriding plate mantle should form, which requires substantial mechanical weakening for strain localization to occur. The metamorphic sole is the ideal place to study subduction initiation, in which the High-Temperature (HT) metamorphic sole records distinct time-temperature conditions from the Low-Temperature (LT) metamorphic sole. Geochronology points out that the HT sole forms before and the LT sole forms during and immediately after subduction becomes self-sustaining. However, the grain-scale deformation mechanisms and rheology of the structurally lower sole unit are poorly constrained, which hinders predictive insight into what deformation-metamorphic processes lead to strain localization during subduction infancy. Here, we apply optical and electron microscopy to naturally-deformed epidote-amphibolites from the Semail Ophiolite (Oman) to infer their rheological behaviors during prograde subduction to P-T conditions of ~7 – 10 kbar, 400 – 550 °C. Epidote-amphibolites are very fine-grained, strongly foliated, and lineated, and commonly exhibit polyphase fabrics in which amphiboles (~10 – 50 μm), and epidotes (~5 – 20 μm) are key strain-accommodating phases. We define three end-member fabric types defined by the relative proportion of strain-accommodating phases, amphibole-rich, epidote-rich, and mixed. Two-point correlation connectivity analysis demonstrates that amphiboles are always interconnected regardless of fabric type, while epidotes are less well-connected in epidote-rich fabrics, but non-connected in mixed-phase fabrics. Electron Backscatter Diffraction reveals Crystallographic Preferred Orientations (CPOs) in amphiboles, high intragranular misorientation angles with subgrain and tilt walls indicative of the easy slip system (hk0)[001], strong Shape Preferred Orientations (SPOs), and High Mean Orientations Spreads (MOS) (~0 – 6°), interpreted as evidence for coupled rigid rotation and dislocation glide. Epidotes, in contrast, record weak CPOs defined by [010] directions aligned with the lineation, low intragranular misorientation angles, moderate SPOs, small grain sizes (~5 – 20 μm), and low MOS (~0 – 2°), which we interpret as deformation by dissolution-precipitation creep. Our observations demonstrate that depending on the phase distributions, bulk epidote-amphibolite rheology could be approximated either as interconnected weak layers defined by amphibole dislocation glide or low-temperature plasticity, or a composite rheology defined by equivalent contribution from plasticity and fluid-assisted, diffusion-accommodated creep. We estimate strain rates from geologic and geochronological data ($6 \cdot 10^{-11}$ to 10^{-12} s^{-1}) and stress estimates from quartz piezometry (11 – 75 MPa), which we use to calculate viscosities in the order of 10^{16} – 10^{18} Pa s. On long-term tectonic timescales (~Myrs), such low viscosities are consistent with these rocks serving as key strain localizing agents during subduction infancy and are one of the parameters that are consistent with the dynamics transition towards self-sustaining subduction. On shorter, seismic to decadal timescales, coupled glide- and diffusional deformation of epidote-amphibolites provide a grain-scale strain-hardening deformation that could lead to cyclic/recurring creep transients in warm subduction zones.

Table of Contents

List of Figures

1. Introduction

One of the primary drivers of tectonic plate movement is the subduction of cold lithosphere into the mantle (e.g. Mueller and Phillips, 1991; Bercovici, 2003; Stern and Gerya, 2018). For subduction to initiate, strain must localize and lead to the formation of a shear zone that accommodates relative plate movement and comprises deformed portions of the uppermost descending slab (metamorphic sole) and the lowermost overriding lithosphere (e.g. Kemp and Stevenson, 1996; Bercovici and Ricard, 2012; Behr et al., 2022). However, the mechanisms facilitating strain localization at the grain scale during the inception of a subduction zone continue to be a subject of controversy, largely because microstructural observations from natural rocks are lacking for key stages of subduction initiation and associative flow laws are not defined for polyphase rocks that form along the subduction interface.

Several plate-to-global scale mechanisms have been proposed to explain initiation and maintenance of subduction zone, which have historically been grouped into *induced* and *spontaneous* end-members (Stern, 2004; Stern and Gerya, 2018). These categories encompass scenarios in which a pre-existing subduction zone was already operating, or a newly-destructive boundary formed, respectively. For the case of *spontaneous*, newly destructive subduction initiation, proposed tectonic configurations include: (1) the gravitational collapse resulting from sedimentary or topographic loading of continental and arc margins (Regenauer-Lieb et al., 2001), (2) the gravitational collapse of transform fracture zones due to lateral thermal buoyancy differences between adjacent oceanic plates of varying ages (Gerya et al., 2008), (3) thermal softening due to interactions between tectonic-magmatic plumes and the lithosphere (Ueda et al., 2008), and (4) the catastrophic mechanical damage due to impact of large asteroids (Hansen, 2007). However, numerical models and force balance calculations repeatedly demonstrate that gravitational collapse is not a viable subduction initiation mechanism at passive margins, because the inherent flexural strength of the lithosphere is too high to yield beneath a continental or sedimentary load of any size (Tharp, 1985; Cloetingh et al., 1989; Gerya, 2022; Li and Gurnis, 2023). Furthermore, while plumes and asteroids may be attractive mechanisms for initiating the very first subduction zone in an earlier hotter, heavily bombarded Earth, these are geologically rare events that are too prescriptive to explain the consistent recurrence of subduction initiation throughout the Phanerozoic. Rather, inherent processes during normal evolution of oceanic crust must repeatedly and consistently overcome any resistance to subduction (Stern and Gerya, 2018).

To understand the mechanics facilitating subduction initiation, it is essential to examine the deformation-metamorphic history of subducted oceanic crustal rocks for constraints into rheological processes operating within the interface shear zone. Below many large, relatively in-tact 'Tethyan-type' ophiolites, thin layers (~10's – 100's m) of high-strain metamorphic rocks, comprising materials from the subducted oceanic slab with or without seafloor sedimentary cover, is tectonically juxtaposed with the deformed base of the oceanic lithospheric mantle, called metamorphic soles. The metamorphic sole is commonly interpreted as a shear zone formed during subduction infancy beneath a proto-forearc spreading center and serves as a record of the deformation history and metamorphic processes that occur between the descending slab and the overriding lithosphere. Microstructural analysis of metamorphic sole rocks can provide insights into strain localization and rheological changes during subduction initiation.

The metamorphic sole comprises two distinct sections: the High-Temperature (HT) and Low-Temperature (LT) metamorphic sole (Searle et al., 1994). Recent geochronological studies indicate that the HT sole forms during the initial stage of underthrusting (Cowan et al., 2014; Agard et al., 2016; Soret et al., 2017), preceding the development of the lithosphere-scaled shear zone defining the subduction zone, whereas the LT sole forms after the formation of this shear zone (Agard et al., 2016; Kotowski et al., 2021). Previous research suggests that thermal-mechanical changes within the metamorphic sole may provide critical insights into strain localization mechanisms (Ambrose et al., 2021; Kotowski et al., 2021; Soret et al., 2022). The rheological characteristics of the LT sole, although yet to be explored, are of particular significance due to the temporal correlation between LT sole formation and the process of ophiolite formation, and may indicate a crucial role in the development of subduction zones (Kotowski et al., 2021). This is taken as evidence that the LT sole forms along the plate boundary at and immediately after the time when vertical driving forces dominate and the subduction system becomes self-sustaining, driven by negative buoyancy and slab pull (Kotowski et al., 2021; Shuck et al., 2022). The Semail Ophiolite in Oman (crystallization age: ~96.4 – 95.5 Ma) is a promising site to study the rheology of the metamorphic sole since it is one of the most extensively studied and documented ophiolites with defined PT conditions and crystallization age constraints (Fig. 1; e.g. Coleman, 1981; Menzel et al., 2020; Godard et

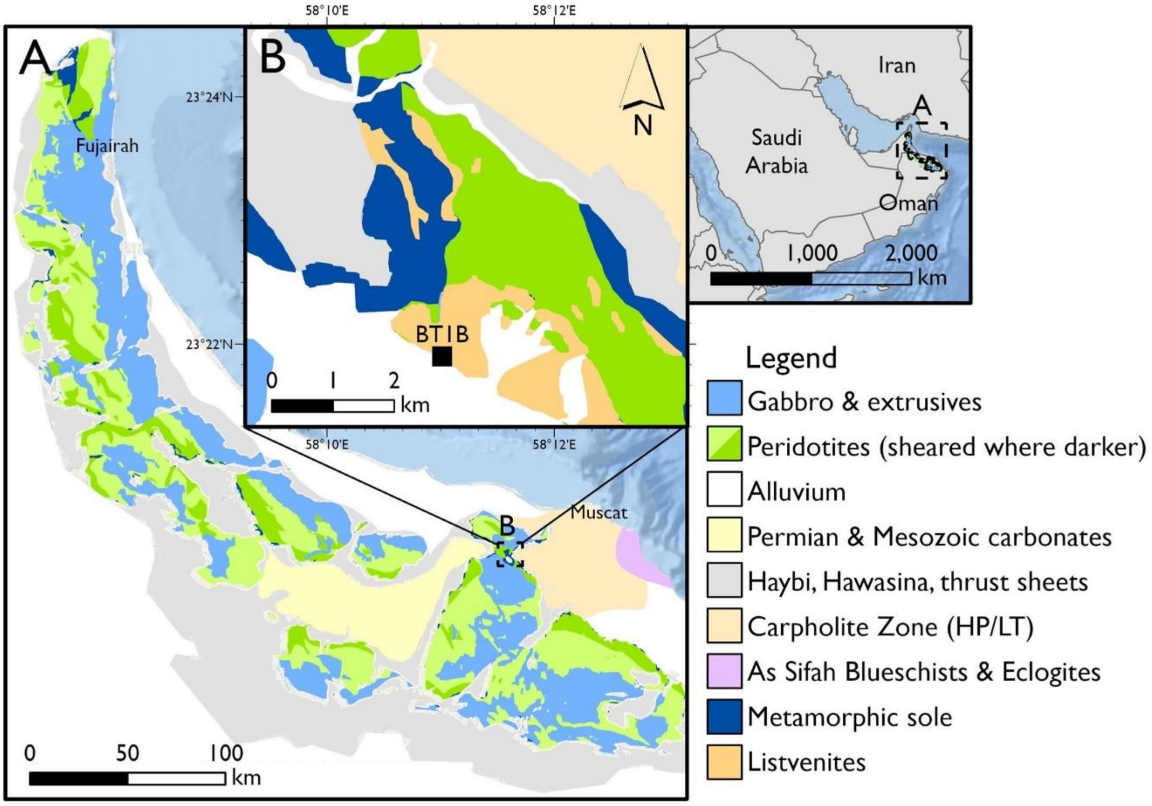

Figure 1 | (A) Geologic Map of the Semail Ophiolite, modified from Agard et al. (2016) and Kotowski et al. (2021). (B) Geologic close-up map of borehole BT1B, modified from Menzel et al. (2020).

al., 2021; Kotowski et al., 2021; Rioux et al., 2023). By leveraging the established thermal and geothermal geochronological context of Oman, I aim to answer the following research question: What deformation mechanism operates in the heterogeneous epidote-amphibole-plagioclase-rich rocks of the LT sole at the onset of self-sustaining subduction?

Here, I investigate the microstructural signatures of subduction infancy recorded by LT sole rocks recovered as part of the Oman Drilling Project (Site BT1B) beneath the Semail Ophiolite. I combine optical and electron microscopy techniques to identify the key strain-accommodating phases in epidote-amphibolites and interpret the dominant micro-physical deformation mechanisms they exhibit, to make a first-order assessment of the rheology of the LT metamorphic sole. Building on previous microstructural and petrologic work done by Kotowski et al. (2021), I target samples with microstructural domains that record prograde subduction (e.g., up-T and up-P, syn-kinematic, foliation- and lineation-defining growth zonations in amphiboles) to minimize effects from retrograde metamorphism and fluid influx. Using Electron Backscatter Diffraction (EBSD), I map the distributions of phases, quantify Crystallographic Preferred Orientation and grain size distribution, and (if present) intracrystalline plastic strain features. My constraints on naturally deformed epidote-amphibolite rock rheology are relevant in other tectonic environments such as mountain belts and the middle crust, and will potentially shed light on the enigmatic, transient creep processes during slow earthquakes, which are prevalent in modern warm subduction zones.

2. Geological Context and Background

2.1. The Semail Ophiolite

The Semail Ophiolite, stretching 500 kilometers along the northeastern edge of the Arabian Plate and covering an area of 20,000 km² with structural massifs reaching 5-7 kilometers in thickness, is primarily situated in Oman but extends into the United Arab Emirates. It is recognized as one of the largest and most extensively studied ophiolites globally (Fig. 1; e.g. Coleman, 1981; Menzel et al., 2020; Godard et al., 2021; Kotowski et al., 2021; Rioux et al., 2023; van Driel, 2023). The ophiolite sequence consists of a substantial mantle section, approximately 9-12 kilometers thick (Nicolas et al., 1988), overlain by a well-preserved layered oceanic crust spanning 4-8 kilometers (Nicolas et al., 1996), which includes lower gabbros to upper volcanics. This sequence formed 96.1 – 95.2 Ma with high-precision U-Pb dating (Rioux et al., 2023). Positioned beneath the ophiolite is a series of underthrust sheets consisting of pelagic and turbiditic sediments, shelf carbonates, and alkaline Haybi volcanics, named the Hawasina group. These formations are remnants of an oceanic basin formed during the Permian to Triassic period due to a mantle plume beneath the region, contributing to the breakup and thinning of the Arabian continental margin (Bechennec et al., 1990; Chauvet et al., 2011). During the late Cretaceous, the ophiolite, along with the underlying allochthonous units, was thrust onto the Arabian platform.

Analysis of the upper volcanics' geochemistry shows high concentrations in compatible elements (Fe, Mg, Mn), low concentrations in incompatible elements (Ba, Sr, Pb), and enrichment in fluid-mobile elements (K, Rb, light rare earth elements). This indicates a shift from oceanic accretion to subduction-related volcanism (Belgrano et al., 2019), interpreted as evidence of subduction initiation, transitioning from mid-ocean ridge settings to intra-oceanic underthrusting (Coleman, 1981; Goodenough et al., 2010) or spontaneously initiating subduction without initial mid-ocean ridge conditions (Searle and Cox, 2002; MacLeod et al., 2013).

Remnants of the metamorphic sole, which is proof for the subduction expected by the geochemical signatures, are found beneath the ophiolitic sequence (Rioux et al., 2023). Comprising metamorphosed mafic oceanic crust along with subordinate metasediments, the metamorphic sole rests upon the base and progresses from HT amphibolite/granulite to LT greenschists facies at the top (Soret et al., 2017; Godard et al., 2021). The HT unit comprises amphibolites with or without garnet and clinopyroxene (Soret et al., 2017; Guilmette et al., 2018; Rioux et al., 2023). The HT sole primarily consists of metamafic rocks in the amphibolite-to-granulite facies containing garnet-clinopyroxene mineral assemblages, with peak PT conditions of ~10 – 14 kbar and ~750 – 850 °C (Cowan et al., 2014; Soret et al., 2017). High-precision U-Pb zircon crystallization ages obtained from plagiogranites and leucocratic lenses within the HT sole indicate ages of ~94.8 to 94.5 Ma (Warren et al., 2005; Rioux et al., 2016), which closely aligns with the timing of ophiolite formation. The similarity of ages between the HT sole formation and the ophiolite sequence supports the interpretation that the Oman Ophiolite originated from spontaneous subduction, with concurrent timing of underthrusting and extension in the upper plate (Searle and Cox, 2002; MacLeod et al., 2013). However, recent Garnet Lu-Hf geochronology demonstrates that metamorphism at high-T conditions occurred at ~104 Ma, i.e. ~8 Myr *before* the crystallization age of the ophiolitic crust (Guilmette et al., 2018; Godard et al., 2021), implying a young and heated overlying mantle lithosphere during sole formation (Guilmette et al., 2018; Godard et al., 2021).

The LT sole consists of both metasedimentary and -mafic rocks recording epidote-amphibolite facies assemblages heavily overprinted by greenschist facies retrogression (Hacker and Mosenfelder, 1996; Kotowski et al., 2021). Recent mineral chemistry and Si-in-phengite and amphiboles of peak epidote-amphibole-plagioclase assemblages yield equilibrium PT conditions of ~7 – 10 kbar and ~450 – 550 °C (Kotowski et al., 2021), which are notably different in pressure estimates from amphibole-plagioclase thermobarometry and Raman spectroscopy on carbonaceous samples with PT conditions of ~4.5 – 5.5 kbar and ~450 - 500 °C (Soret et al., 2017). Syn-kinematic titanite porphyroblasts in interlayered calc-schists yield U-Pb crystallization ages of ~91 ± 3 Ma, i.e. overlapping with the crystallization of the ophiolitic crust but trending several million years later and ~13 Myr *after* the crystallization ages of the HT sole (Kotowski et al., 2021). This suggests that while both the LT and HT soles reached similar depths, the LT sole experienced these conditions at cooler temperatures and at a later time (Kotowski et al., 2021).

2.2. Sub-ophiolite LT metamorphic rocks at OmanDP Site BT1B

The Oman Drilling Project (OmanDP) served as a collaborative initiative aimed at unraveling the processes shaping and altering oceanic crust and mantle. In March 2017, at Site BT1B (Fig. 1B), 300 meters of core material were sampled with a 100% recovery rate (Fig. 2). This core primarily encompasses 196 m of mantle rocks, exhibiting localized mylonitic features and is predominantly composed of listvenites (carbonated peridotite) with relict serpentinite lenses. The main constituents comprise magnesite, serpentinite, and quartz, with lesser quantities of dolomite and oxides (Menzel et al., 2020; Godard et al., 2021).

Directly beneath this section is the Basal Thrust fault zone, characterized by a roughly 40-centimeter-thick layer consisting of fault gouge and ultracataclasites (Kotowski et al., 2021). Kotowski et al. (2021) noted that the original thrust fault was likely reactivated as a normal fault, consistent with outcrop-scale observations of low-extensional features (Menzel et al., 2020) and the notable absence of the HT sole. Below this ultracataclastic zone lies a 104-meter layer of the LT metamorphic sole (Fig. 2). The upper portion of the LT sole is a 34-meter thick, phyllitic, very fine-grained blue-gray to gray-green meta-sedimentary unit. These rocks are rich in micas, quartz, oxides, and contain small amounts of epidote, and comprise mm-to-cm thick calcite-bearing layers where titanites contain sufficient U for U-Pb geochronology (Kotowski et al., 2021).

Below the meta-sedimentary unit is a 60-meter-thick layer of schistose meta-mafic rocks displaying mm-to-cm-scale laminations of dark green-gray and pistachio green-yellow layers. This distinctive compositional banding reflects amphibole-rich layering with epidote and plagioclase)-rich and epidote-rich layering with amphibole, plagioclase, and quartz, respectively. These layers also contain minor amounts of titanite, chlorite, paragonite, hematite, micas, and apatite (Godard et al., 2021; Kotowski et al., 2021).

The lowest 10 meters of the core comprise fine-grained, blue-black, amphibole-dominated schists with a strong foliation most clearly visible as mm-scale, rootless isoclinal folds in light gray-white plagioclase and epidote layers (Kotowski et al., 2021). Throughout the metamorphic sole, ductile fabrics are cross-cut by several larger brecciated horizons (the absolute widths of which cannot be constrained due to limits of core-scale observations) and multiple sets of micro-faults, often accompanied by narrow cataclastic zones (Kotowski et al., 2021). Younger normal micro-faults with calcite indicate that after the underthrusting of the Arabian continental margin, brittle extension led to some exhumation of the ophiolite. CO2-rich fluids might have come from local calcareous strata in the metasedimentary section or the underlying carbonate platform sediments (de Obeso and Kelemen, 2018).

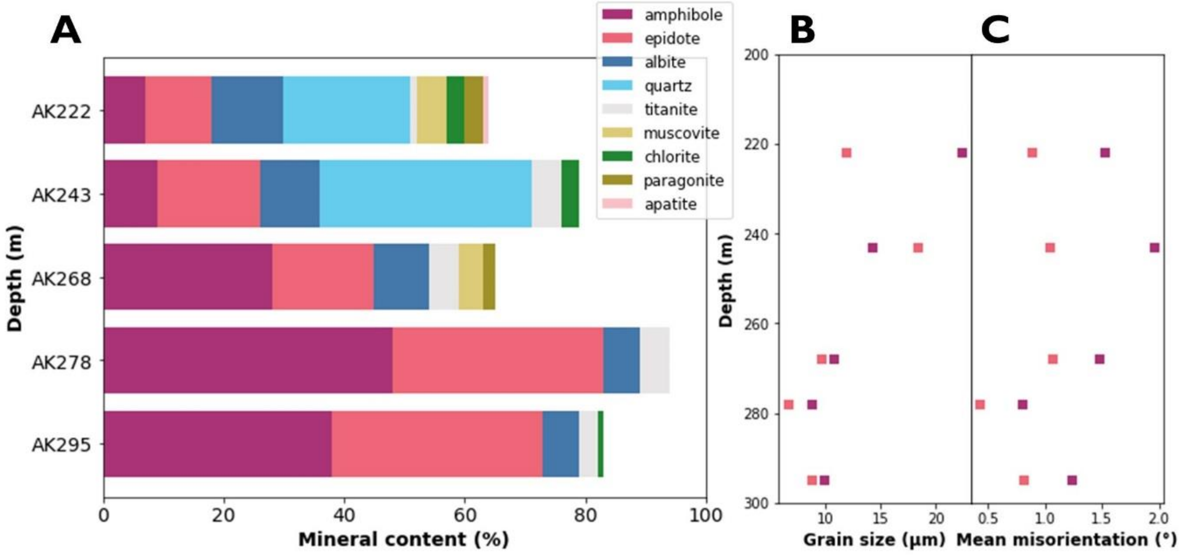

Figure 2 | (A) Mineral content of all measured EBSD sections, see Fig. S1 for locations on thin sections. Non-indexed mineral proportion mainly consists of chlorite and micas. (B) Mean grain size for amphibole (purple) and epidote (pink) for each EBSD section. (C) Mean misorientation (MOS) of amphibole (purple) and epidote (pink) for each EBSD section. Thin section numbers correspond to the depth in meters of borehole BT1B.

2.3. Previous constraints on (epidote-)amphibolite rheology

Observations from nature and experiments demonstrate that amphiboles in greenschist-to-amphibolite (medium to high-temperature) metamorphic facies rocks exhibit a range of deformation behaviors, but the factors that control operative deformation mechanisms remain poorly constrained. For example, Wang et al. (2021) presented structural and petrologic observations from the eastern Himalayan syntaxis and interpreted with axial compression experiments and EBSD that amphiboles locally exhibit dynamic recrystallization accommodated by dislocation creep. This is supported by Pearce et al. (2011), which showed that dislocation creep (600 °C, 8 – 9 kbar) in intrusions in amphiboles in the Lewisian Complex, NW Scotland, is related to the distribution of amphiboles relative to other phases because dislocation-based mechanisms were only evident where amphiboles defined a load-bearing framework (Handy, 1989). In contrast, Getsinger et al. (2013) presented deformation experiments on 'common' amphiboles that highlighted the significance of secondary phases because amphiboles contained in mixtures of foliation-forming amphibole and plagioclase exhibit lineation-defining compositional growth zonations and extremely fine-grain sizes, consistent with deformation by diffusion creep/dissolution precipitation creep.

Experimental work demonstrates that temperature and deformation rate also clearly influence epidote-amphibolite rheology, in that relatively cool temperatures and fast rates usurpingly favor brittle deformation (Okazaki and Hirth, 2020). Studies based on natural samples, however, which experienced strain rates ~4 – 6 orders of magnitude slower than experiments, consistently demonstrate plastic mechanisms over a range of deformation temperatures. For example, Stokes et al. (2012) studied amphibolites from metavolcanic and metasedimentary rocks from the Eastern Blue Ridge, North Carolina (400 – 700°C, 8.5 – 10 kbar), and demonstrated that at geological strain rates and temperatures of ~500 – 750°C, rocks deform by dissolution-precipitation processes, as indicated by the preservation of fabric development inside grains. However, under higher temperatures, as recorded by amphibolites from Diancang Shan, China (580 – 680°C, 5 – 6 kbar), amphiboles exhibit dominantly dislocation creep as indicated by well-defined CPOs, subgrain walls, and high intragranular misorientations in the grains (Cao et al., 2010). This has been interpreted as evidence that higher temperatures can facilitate some intracrystalline diffusion and climb to account for recovery that is needed for dislocation-based mechanisms to efficiently accommodate strain, whereas, under lower temperatures where more fluids are abundant and volume diffusion is sluggish, dissolution-precipitation creep is easier (Jung et al., 2021).

The distinction between dislocation-based and diffusion-based mechanisms is crucial because these grain-scale physical processes require different activation energies and stresses to operate and exhibit different grain size sensitivities and therefore will control the style of strain localization during shear zone evolution. Many natural studies have demonstrated that dislocation creep and resulting grain size reduction can lead to rock weakening and strain localization (e.g. Warren and Hirth, 2006), but more typically, deformation concentrates in zones where stresses are too low for crystal plastic mechanisms to operate (Bercovici and Ricard, 2012; Wassmann and Stöckhert, 2013). Therefore, microstructures characterized by phase mixing and phase pinning, thereby capable of keeping grain sizes small, may be a prerequisite for the strain localization required for the generation and maintenance of plate tectonics (Bercovici and Ricard, 2012).

Metamorphic soles are ideal natural laboratories for investigating amphibolite rheology during plate boundary development (Soret et al., 2019; Agard et al., 2020; Ambrose et al., 2021; van der Wurf, 2023), since past work has shown that amphibole-rich sole rocks exhibit shifts in deformation mechanisms through time as temperature, secondary phases, and fluid conditions evolve. For example, Ambrose et al. (2021) highlighted the significance of prograde dehydration and grain coarsening for favoring dislocation creep in granulites during subduction initiation in the Oman HT sole at the Masafi window. Moreover, Soret et al. (2019) studied rocks from a similar structural level at Wadi Tayin, Sumeini, and Asimah Khubakhib, and interpreted that initial HT sole deformation is characterized by dislocation creep in pyroxene, coupled with brittle fracturing, fluid ingress, and dissolution-precipitation of hornblende, which then provides a weakening mechanism leading to strain localization (cf.

Agard et al., 2020). However, Van der Wurf (2022, UU MSc Thesis) argued that hornblendes in HT sole rocks from Mont Albert, Quebec were too coarse-grained to accommodate *significant* strain by dissolution-precipitation, grain-size sensitive creep, and rather they exhibit dynamic recrystallization and minor grain size reduction by dislocation creep. However, there was no clear evidence for viscous strain localization as a consequence of hornblende grain size reduction, indicating that some other mechanism or lithological unit must contribute to strain localization during subduction infancy, and suggested that further analysis of LT sole rocks was needed to evaluate their possible contribution as strain localizing lithologies.

While many rocks can be simplified to a single dominant mineral phase that dictates the foliation and can thus be entirely understood by the rheological characteristics of that mineral, in cases where multiple minerals are equally prominent or the dominant phase is unclear, it becomes imperative to consider the combined behavior of these phases. This is because each mineral may exhibit different deformational behaviors (Brodie and Rutter, 1985; Jordan, 1988; Handy, 1989). While amphiboles have been studied in multiple researches, there has been relatively little research conducted on epidotes. Epidotes in blueschists have been investigated by De Caroli et al. (2024). The authors showed a block-in-matrix association, in which the blocks show a poorly developed foliation and CPO compared to the matrix. Both matrix and block rheology is controlled by diffusion and reaction creep in glaucophane and albites, while dislocation creep was observed in the relatively rigid epidote (De Caroli et al., 2024). However, the epidote-amphibolite LT sole rocks differ from these studies.

3. Materials and Methods

3.1. Sample selection and process

I selected a subset of five meta-mafic thin sections obtained from borehole BT1B used for Kotowski et al. (2021) that document prograde, syn-subduction, deformation, and metamorphism during progressive increase in pressure and temperature (Fig. S1). These samples contain amphibole zonation characterized by increasing Al_2O_3 and TiO_2 contents from core to rim, decreasing Mg#, decreasing Si apfu, and increasing Na/(Na + Ca). We attempted to avoid retrograde mineralogical and microstructural overprints in order to assess plate interface rheology during subduction.

Through optical microscopy, I identified the primary phases accommodating strain in LT sole rocks and documented microstructural evidence for intracrystalline plastic and/or diffusional strain to qualitatively determine operative strain-accommodating mechanisms. For example, I documented features such as undulose extinction and grain boundary shapes; presence and absence and geometry of subgrains; geometry, orientation, and sharpness of subgrain walls; and presence or absence and shapes of chemical zoning relative to the foliation and lineation. I selected areas in the thin sections where the matrix was representative and devoid of later-stage veins unrelated to subduction and targeted these regions with Electron Backscatter Diffraction (EBSD) analysis. The goal was to map phase distributions, assess Crystallographic Preferred Orientation (CPO), grain size distribution, and, where applicable, features indicating intracrystalline plastic strain, to provide quantitative confirmation and/or alternative insights compared to deformation mechanisms hypothesized from optical microscopy.

3.2. Materials

Five fine-grained, meta-mafic thin sections of the LT metamorphic sole have been extracted from hole BT1B, from 222, 243, 268, 278, and 295 meters depth in the core (Fig. 2 and S1). In all LT sole samples described herein, amphibole and/or epidote are the two volumetrically dominant strain-accommodating foliation-defining minerals. I only address vein-forming minerals where they are clearly deformed and transposed into parallelism with the dominant foliation and therefore experienced similar deformation histories.

AK222 is a metamafic lens situated in the metasedimentary segment of the borehole. This lens is defined by a matrix dominated by ~200 μm albite crystals, ~50 μm epidote grains, ~80 μm albite grains, and ~80 μm chlorite. Porphyroblasts are contained within the matrix of ~1 mm blue-green amphibole (edenite/pargasite) and ~200 μm muscovite. Amphibole porphyroblasts manifest as solitary, single arranged sub-to euhedral entities. These crystals align either parallel or at a slight angle to the foliation and contain inclusions of epidote, quartz, chlorite, albite, and titanite. Epidotes, especially those in larger grains, exhibit inclusions of albite, titanite, quartz, and amphibole. Chlorite, titanite, and amphiboles have been identified on the rims of epidote grains. Typically, epidotes demonstrate high relief in plane-polarized light (PPL); however, some grains exhibit weak relief in PPL, revealing chemical zoning with rainbow coloring in XPL. No chemical zoning is observed in amphiboles in XPL. The matrix contains ~0.9-2.6 mm thick sheared quartz veins, locally with sub-mm thick chlorite rims Younger quartz and carbonate veins intersect the matrix at high angles (~40°) to the foliation.

AK243 is in the metamafic portion of the core in which the matrix is characterized by oriented folded ~300 µm edenite, ~200 µm chlorite, ~85 µm epidote. Subsections in this thin section display the same amphibole porphyroblast behavior as in AK222. The matrix is followed by the transition from a ~1 cm thick quartz and albite (±epidote and amphibole) vein to a foliated matrix comprising edenite, chlorite, epidote, and titanite, all with the long crystal axes aligned and defining a macroscopic lineation. Inclusions for amphiboles and epidotes, as described in AK222, are the same in these thin sections, but found in a lesser extent. An amphibole-rich margin surrounds the quartz-albite vein, transitioning to a medium-grained (~100 µm,) chlorite-epidote-titanite compositional band. Adjacent to this compositional band, there is a gradational transition over a ~cm to a fine-grained matrix The titanite content increases progressively further away from the vein. Semi-brittle micro-faulting has an offset between the matrix and the vein.

AK268 consists of a fine-grained ~20 µm epidote, ~120 µm amphibole (hornblende), ~100 µm albite schist intersected by ~75 µm width Fe-Ti oxides, chlorite, and carbonate seams. Within amphibole-dominated fabrics, larger crystals of approximately 0.1 mm define the foliation direction, while smaller grains (~20 µm) within these layers exhibit a greater tendency to deviate from the foliation, occasionally aligning orthogonally to it. Inclusions for amphiboles and epidotes, as described in AK222, are the same in these thin sections. Grains within amphibole-rich fabrics generally display sub- to euhedral morphologies, whereas single amphibole grains within epidote-dominated fabrics are predominantly anhedral, indicative of breakdown through mineral reactions. Part of the thin section is heavily carbonated and exhibits ~cm wide calcite veins parallel to the foliation, or ~cm wide quartz-albite veins parallel with the foliation with ~0.5 mm sized epidote crystals grew from fluid.

AK278 is characterized by an epidote-rich foliation defined by alternating bands of oriented ~20 µm epidote grains and ~300 µm pargasite/edenite grains; and an epidote-albite-rich matrix containing ~80 µm epidote, ~60 µm quartz, ~300 µm calcite aggregates. This compositional banding is cross-cut by calcite tension gashes, exhibiting ~200 µm brittle offset. The epidote-rich matrix is characterized by alternating bands of ~1-4 mm of both mainly epidote and mainly amphibole, with lesser amounts of ~50 µm titanite in both zones. Sub-sections of these thin sections display the same amphibole-rich foliation as described in AK268. Epidotes in epidote-rich fabrics align with the prevailing foliation, although to a lesser extent compared to stretched-out amphibole grains. Consequently, a considerable proportion of the epidote grains deviates from foliation alignment. These grains display subhedral to anhedral morphologies, adopting columnar-like structures. Inclusions for amphiboles and epidotes, as described in AK222, are the same in these thin sections.

AK295 is a deformed fine-grained amphibole (hornblende) and epidote-rich amphibolite. Grain sizes in the matrix are ~10 µm for epidotes, and ~20 µm for oriented hornblende, only a few ~20 µm titanites and ~20 µm albites have been observed. Sub-sections of these thin sections display the same amphibole- and epidote-rich fabrics as described in AK268 and AK278, but are more folded than in those thin sections. Inclusions for amphiboles and epidotes, as described in AK222, are the same in these thin sections. Veins have axial planes parallel to the dominant foliation which contains very fine-grained ~1 mm width ~10 μm epidote veins as well as ~1 mm width albite-chlorite-epidote veins. The epidote veins have their grain sizes comparable to those in the matrix.

3.3. Quantitative microstructural analysis

Electron Backscatter Diffraction (EBSD) acquisition and data processing

Microprobe-polished thin sections were syton polished with colloidal silica, performed with Tegramin-30 for 20 minutes at 5 N, to chemically abrade and smooth surface damage. EBSD data were acquired utilizing a Zeiss Gemini 450 SEM equipped with an Oxford Symmetry Detector and Aztec 5.1 software. The EBSD acquisition parameters encompassed a 20 kV accelerating voltage, 20 nA beam current, an approximate 20 mm working distance with a step size ranging between 0.65 and 1.5 μm, a 70° specimen tilt. Frame averaging (2x) was sometimes used to improve signal intensity and pattern-matching statistics.

Post-processing in Aztec Crystal 2.0, included initial removal of erratic spikes followed by an iterative (maximum of 10 cycles) extrapolation based on the six nearest neighbors (Fig. S2). To eliminate twinning artifacts, pseudo-symmetry elimination was applied to epidote (180° around <301>, <003>, and <-30-1>) and quartz (60° around <0001>), which is in line with Faul (2021) and Hamers et al. (2023). I identified these twin systems by plotting Inverse Pole Figures (IPFs) for the different minerals with Disorientation Axes for Crystal Coordinates in the sample and Disorientation Angle histograms for the 'raw' (pre-pseudo symmetry merged) data. I then compared the data density in the IPFs which show point maxima for recurring axes of rotation, with histograms of disorientation angles. I identified disorientation angles that returned abnormally high histogram densities at angles corresponding with obvious crystal symmetry and then returned to IPF plots for those particular crystal disorientation angles to determine which axes of rotation accommodated apparent twin rotations.

I used Aztec Crystal to produce phase maps, IPF coloring maps, Grain Reference Orientation Deviation (GROD) angle maps, grain size distribution, and mean orientation spread (MOS) distributions from the twin-merged data. Some thin sections have extremely fine-grained fabrics and the lineation was difficult to see when preparing thin sections. I performed a first-pass visual inspection of amphibole [001] directions in pole figures to identify samples that were not sectioned perfectly parallel to the lineation. 3 samples (AK222, AK268, and AK295), the [001] axes clustered at an oblique angle to the conventional EBSD X-direction (horizontal), so I applied a small data rotation to better align the pole figures with the lineation. Data rotation is justified because it allows better visualization of pole figure geometries for (100), (110), and (010) directions relative to the strength of [001] clusters.

Mean grain size and standard deviation were calculated as equivalent circle diameter (cf. Lopez-Sanchez, 2020), internal misorientations, and grain aspect ratio calculations were conducted on grains comprising more than 8 pixels. This criterion dictated that at least 85% of an investigated area must be indexed, following methodologies of Humphreys et al. (2001) and Behr and Platt (2011).

I generated pole figures with MTEX v5.10.2 for bulk rock point-per-grain CPO of strain-accommodating phases and calculated M- and J-indices (Skemer et al., 2005; Bachmann et al., 2010; Mainprice et al., 2015), to quantify the strength of bulk CPO. Single-grain maps and CPO have been retrieved by selecting grains from the interactive phase maps available in MTEX. Slip systems have been read off manually from pole figures consisting of orientations of all pixels in one grain. The slip plane is where the grains are closest to the Y-direction or within the YZ plane, the slip direction is closest to the X-direction, and the rotation axis is the smallest cluster.

Quartz piezometry

We leveraged the experimentally- and theoretically-calibrated piezometric relationship between dynamically recrystallized grain size and subgrain size as a function of quartz flow stress to provide an upper boundary on epidote-amphibolite stress. Available quartz includes quartz deformation experiments coupled with optically-measured recrystallized grain size (Stipp and Tullis, 2003); the same experimental samples from Stipp and Tullis (2003), but with an updated calibration from higher-resolution, EBSD-derived recrystallized grain sizes (Cross et al., 2017); and subgrain width piezometry (Goddard et al., 2020). All piezometers utilize the arithmetic mean of a given 'domain' diameter, either defined as grains separated by misorientations >10°, or subgrains defined as misorientations from >1° (this measurement, therefore, accounts for intracrystalline tilt walls as well as grain boundaries >10°). Moreover, the recently updated EBSD-calibrated recrystallized grain size piezometer from Cross et al. (2017) presented a method to distinguish between relict and recrystallized grains based on mean internal misorientations, effectively extracting a subset of dynamically recrystallized grains with very low internal misorientations, thereby excluding relatively large porphyroclasts that are in the process of recrystallizing. The subgrain size piezometer, on the other hand, extracts measurements via the linear-intercept method. This method allows for quantifying misorientation boundaries that do not fully close within a grain interior.

Grain and subgrain size measurements were conducted on dynamically recrystallized quartz veins in two thin sections that contained enough quartz grains to yield a statistically robust arithmetic mean and standard deviation (minimum ~100 (sub)grains). Following the methodology by Cross et al. (2017), I first plotted histograms of the cumulative number of quartz grains versus mean internal misorientation from low to high using Grain Orientation Spread (GOS) parameter in AztecCrystal. According to Cross et al. (2017), the threshold between relict and recrystallized grains is determined by the knee in the grain number versus the mean GOS curve. Then, taking the mean recrystallized grain size from the subset of recrystallized grains, I used the revised stress-grain size calibration from Cross et al. (2017):

$$D = 10^{4.22\pm0.51}\sigma^{-1.59\pm0.26} \qquad (1)$$

Notably, for the same average grain size, the calculated stress values overlap with those derived from the original Stipp and Tullis calibration.

For comparison, we also determined average subgrain sizes according to the methodology proposed by Goddard et al. (2020). I made EBSD maps with special boundary orientations between 1-10° and >10°, then a grid was placed with ~0.2 mm spacing on the sample horizontally, vertically, and diagonally (45°) on the quartz vein, from which I counted the number of special boundaries (subgrains and grains) that are passed by on a grid divided by the length of the grid. This results in ~50 lines of subgrain sizes for each quartz vein, from which I used the mean subgrain size from Goddard et al. (2020) with provided calibration of Holyoke and Kronenberg (2010):

$$\frac{D}{b} = 10^{0.6\pm0.7}\left(\frac{\sigma}{\mu}\right)^{-1.2\pm0.3} \qquad (2)$$

in which b = 0.51 nm and μ = 42.0 GPa for quartz.

3.4. Grain connectivity analysis

We used 2-point correlation functions to quantitatively describe how well the major strain-accommodating minerals amphibole and epidote are interconnected in these polyphase rocks. This analysis is motivated by Handy et al. (1989, 1994) who demonstrate that two-phase rock rheology can be simplified and approximated by the rheology of the main interconnected weak or framework-forming strong phase if that mineral is sufficiently connected to support the externally applied stress "homogeneously" throughout the microstructure.

EBSD-derived phase maps constructed in Aztec crystal were made binary with ImageJ, so that only amphibole or epidote were color-coded, and all other phases in the rock can be ignored. Following methodology of Amiri et al. (2023), we first conducted a Representative Elementary Size (RES) analysis on full images to determine which pixel size was representative to accurately apply the 2-point correlation function (Fig. S3 and S4). For all samples, we settled on the same pixel size (1 pixel ≈ 4 μm) to facilitate direct comparisons with equivalent analysis resolutions. After rescaling the images to 1000x1000 pixels and selecting a representative squared area of the foliation, we calculated *C2* and *S2* point correlations (Amiri et al., 2023). *S2(r)* is the most commonly used microstructural correlation function, which is the probability that two random points of a certain distance *r(px)* are the same phase, but these two identical phases do not necessarily need to be physically connected (Sheehan and Torquato, 2001; Chen et al., 2020). *C2(r)* is similar to *S2*, but the two random points of a certain distance *r(px)* are not only needed in the same phase but also connected, without other phases dissecting or interrupting the continuous connectivity of the analyzed phase (Jiao et al., 2008; Chen et al., 2020). Finally, using the MorphoLibJ package in ImageJ, I applied connected components labeling (connectivity = 4) to qualitatively visualize the connected parts of a certain phase (Legland et al., 2016) and complement the quantitative analysis.

4. Results

4.1. Microstructural Overview

Qualitative distinctions of fabric types

Four main fabric types occur on mm-to-cm length scales in all analyzed samples (Figs. 3 – 7 and S1): (1) amphibole-rich compositional layers, (2) epidote-rich compositional layers, (3) polyphase epidote-amphibole-albite-rich matrix, and (4) transposed quartz veins. I analyzed

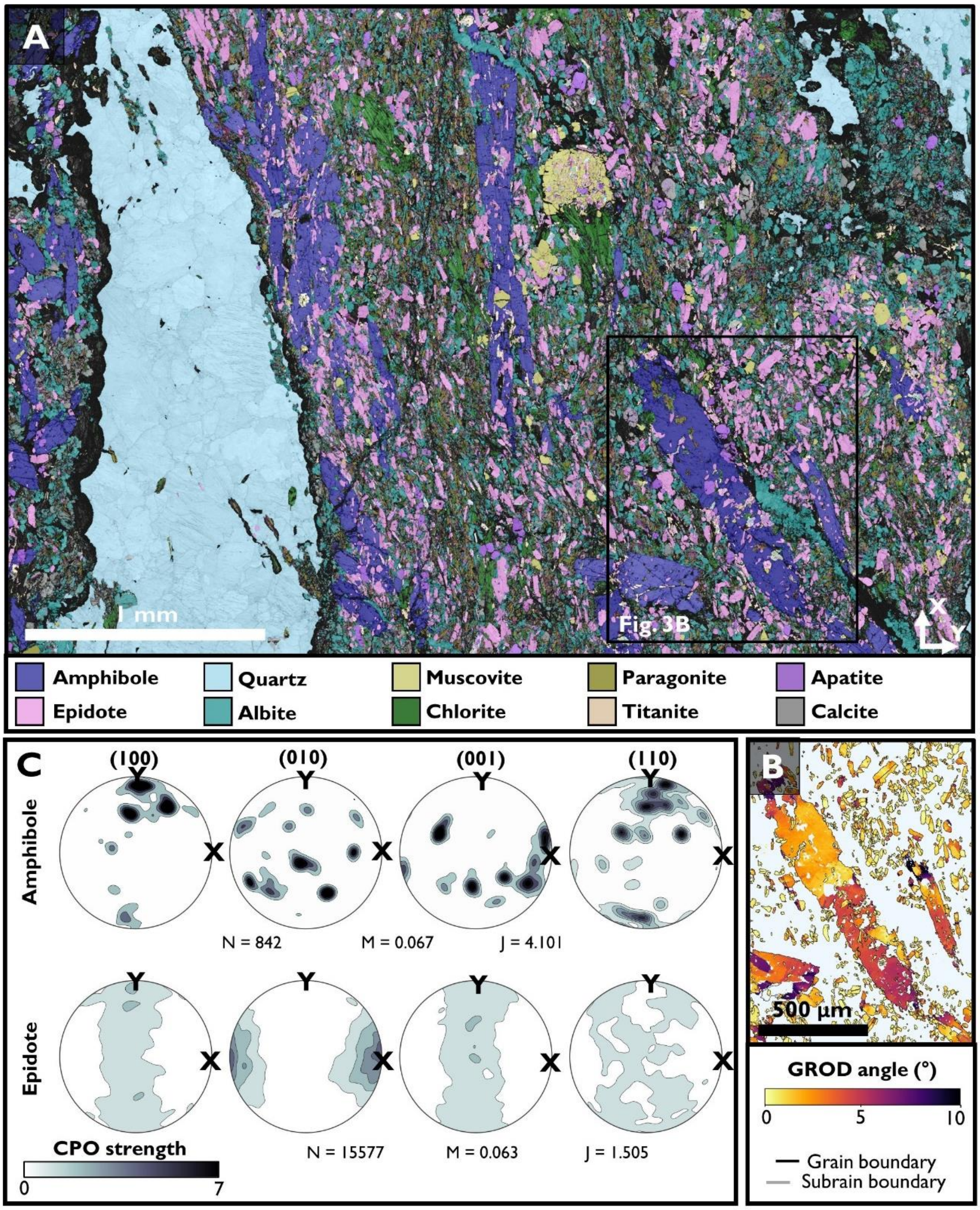

Figure 3 | Microstructural summary of EBSD section AK222. (A) Phase map distributions exhibiting fabric type-Q and type-AE (see text for explanation). (B) GROD angle map of a close-up showing amphibole and epidote internal misorientations. (C) CPO pole figures of amphibole and epidote from all grains of the EBSD section.

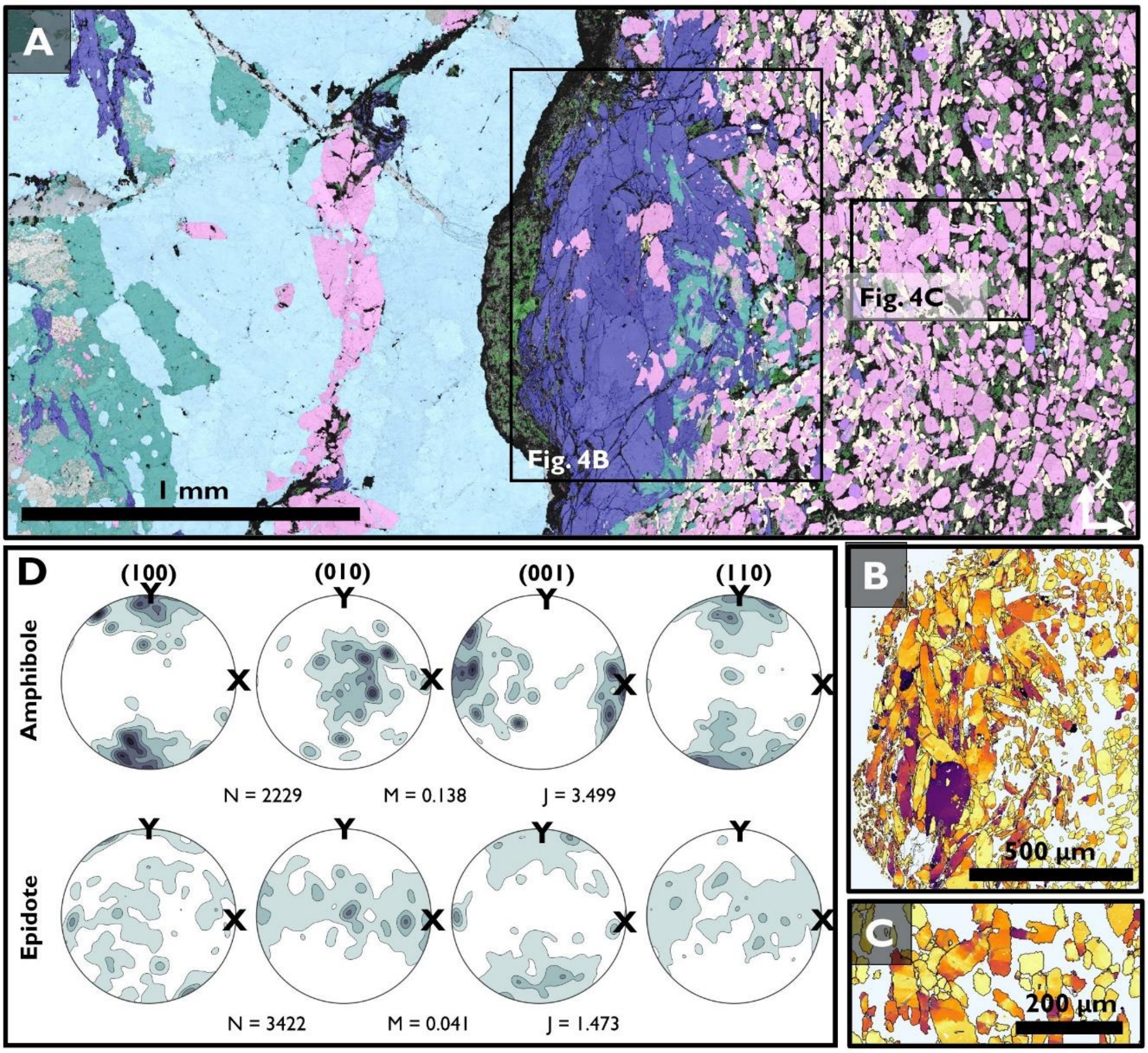

Figure 4 | Microstructural summary of EBSD section AK243. (A) Phase map distributions exhibiting fabric type-Q and type-E (see text for explanation). (B) GROD angle map of a close-up showing amphibole internal misorientations. (C) GROD angle map of a close-up showing epidote internal misorientations. (D) CPO pole figures of amphibole and epidote from all grains of the EBSD section. For legends, see Fig. 3.

each fabric type to investigate the influence of phase distributions and the presence/absence of secondary phases on epidote-amphibolite rheology.

Amphibole-dominated fabrics (herein called fabric type 'A' for amphibole) contain >75 amphibole and are best expressed in AK278 and AK295 (Figs. 6 and 7) in which straight (AK278) or isoclinally folded (AK295) compositional bands of 100 – 1000 µm amphibole grains are well-aligned and define the main foliation. Amphiboles in type-A fabrics are typically elongated and subhedral in morphology. Most grains' long axes are oriented within 10 degrees from the lineation direction; however, some amphibole grains are oblique (~45°) or even perpendicular to the foliation direction. Within and surrounding the amphibole-dominated foliation, clusters of equant, euhedral epidotes, subhedral albites, quartz, and titanites with similar grain sizes (~5-8 µm) are dispersed. Chlorite and other white micas are locally present and contribute to the strong lineation; in AK295, for example, chlorite overgrowths on amphiboles form syn-kinematic fibrous tails with long axes growing parallel to the lineation.

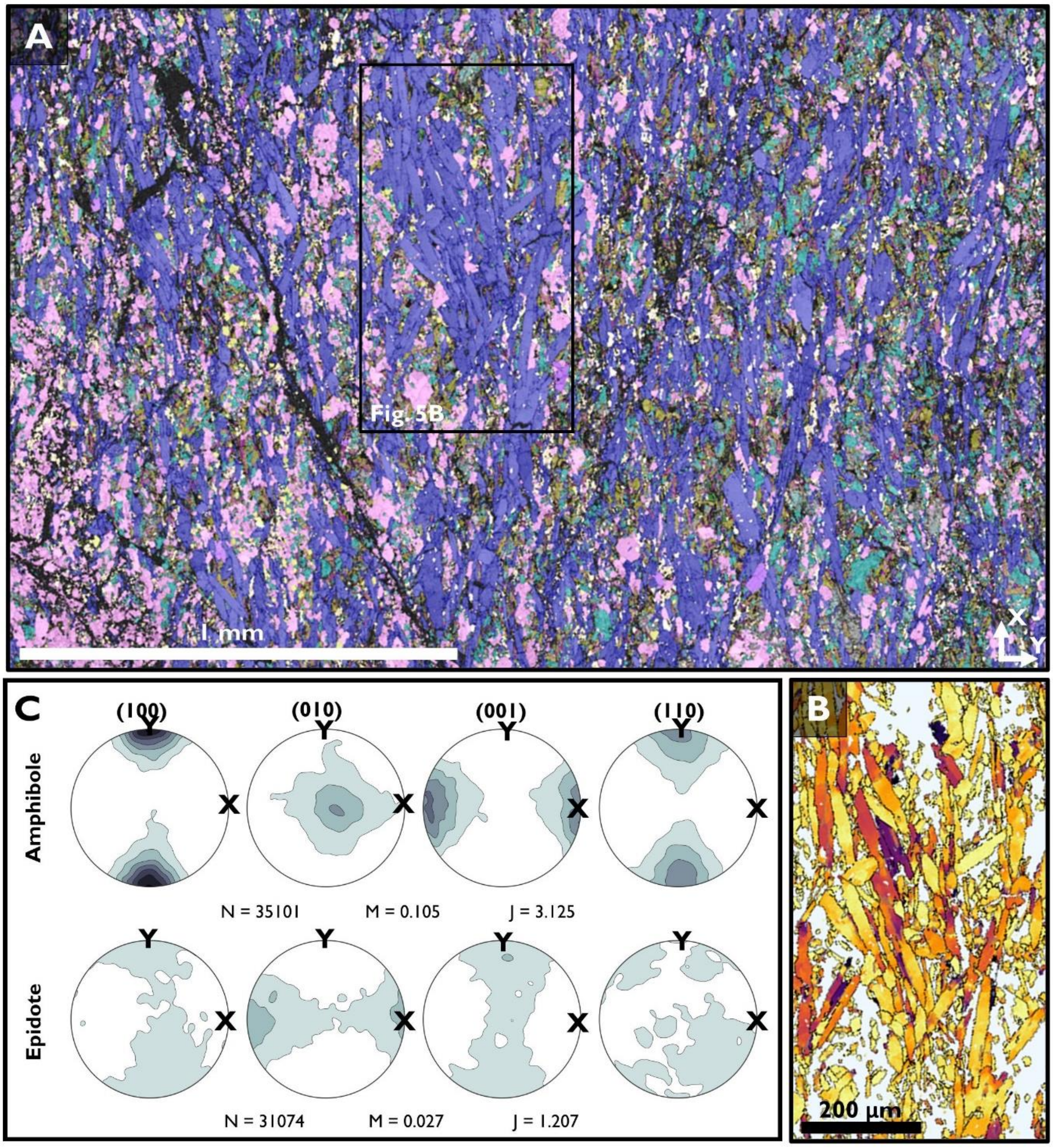

Figure 5 | Microstructural summary of EBSD section AK268. (A) Phase map distributions exhibiting fabric type-AE (see text for explanation). (B) GROD angle map of a close-up showing amphibole and epidote internal misorientations. (C) CPO pole figures of amphibole and epidote from all grains of the EBSD section. For legends, see Fig. 3.

Fine-grained (<2 µm) inclusions of epidotes, quartz, chlorite, albite, and titanite are observed inside the amphiboles.

Epidote-dominated fabrics (herein called fabric type 'E' for epidote) contain >75% epidote, are commonly found together with fabric type-A (e.g. AK278 and AK295), and are defined by compositional bands of 100 – 500 µm. Epidotes in type-E fabrics are not as prominent a shape-preferred orientation but where epidotes do have long axes they are rotated and aligned roughly with the lineation direction. Within and surrounding the epidote-dominated fabric, clusters of subhedral amphiboles, albites, quartz, and lesser amounts of titanites are observed with similar grain sizes (~4-9 µm). Epidotes, especially those in larger grains, exhibit <2 µm

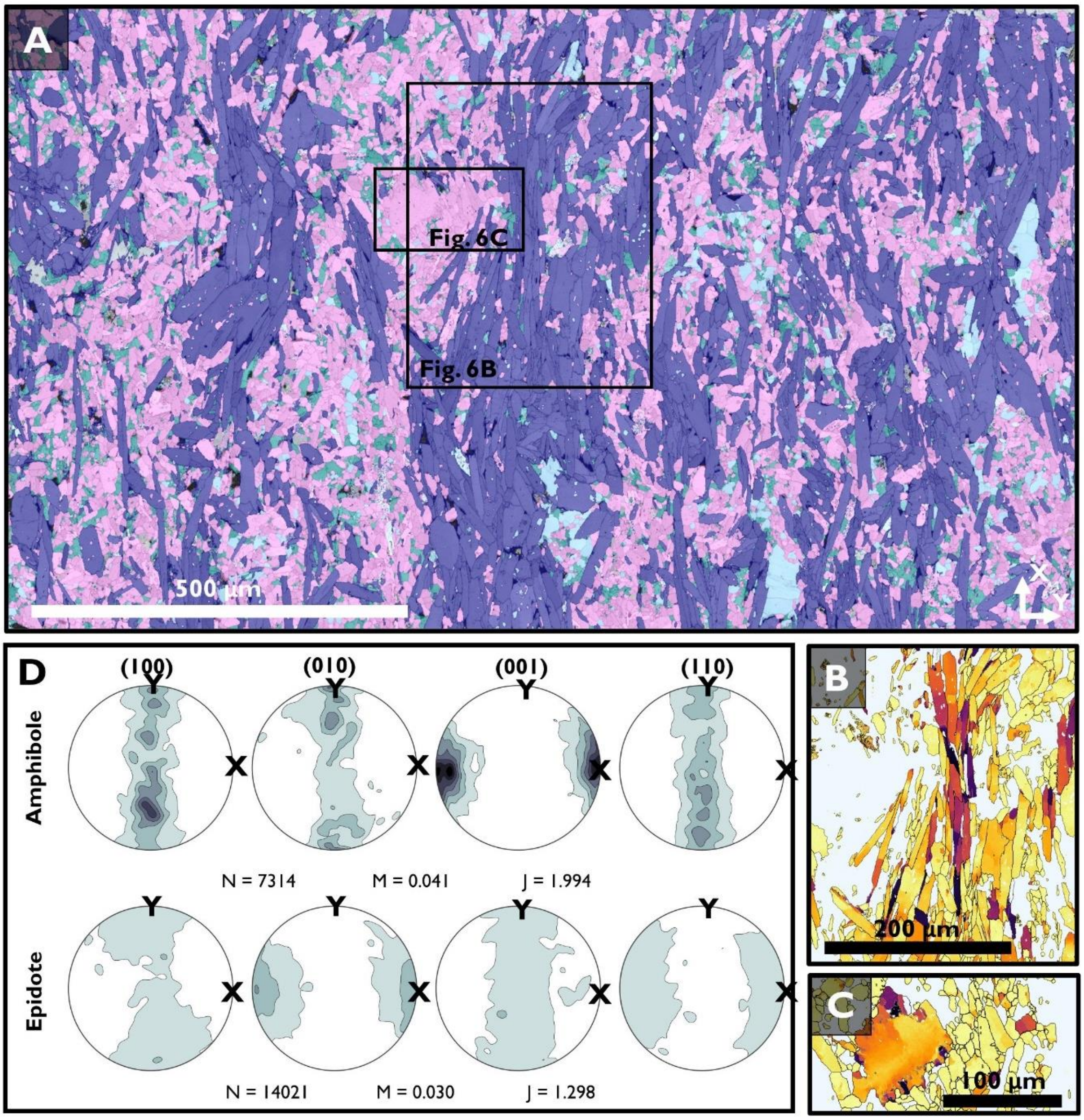

Figure 6 | Microstructural summary of EBSD section AK278. (A) Phase map distributions exhibiting fabric type-A and type-E (see text for explanation). (B) GROD angle map of a close-up showing amphibole internal misorientations. (C) GROD angle map of a close-up showing epidote internal misorientations. (D) CPO pole figures of amphibole and epidote from all grains of the EBSD section. For legends, see Fig. 3.

inclusions of albite, titanite, quartz, and amphibole. In sample AK243, type-E fabrics comprise roughly euhedral epidote grains (~12 µm) that are fully surrounded by chlorite and titanite, which we interpret as a recrystallized vein and therefore do not consider as matrix-defining foliation (Fig. 4). Thin sections with both types A and E consist of more than 70% of amphiboles and epidotes (Fig. 2).

Mixed amphibole-epidote fabrics (herein called fabric type 'AE') comprise 20 – 60% amphiboles + epidotes by thin section area, in addition to the presence of 40 – 80% other minerals, namely albites and (white) micas (paragonite and muscovite), chlorite, and apatite. Type-AE fabrics are best expressed in AK222 and AK268 (Figs. 3 and 5) and do not show a clear distinction in compositional banding dominated by amphiboles or epidotes but are rather

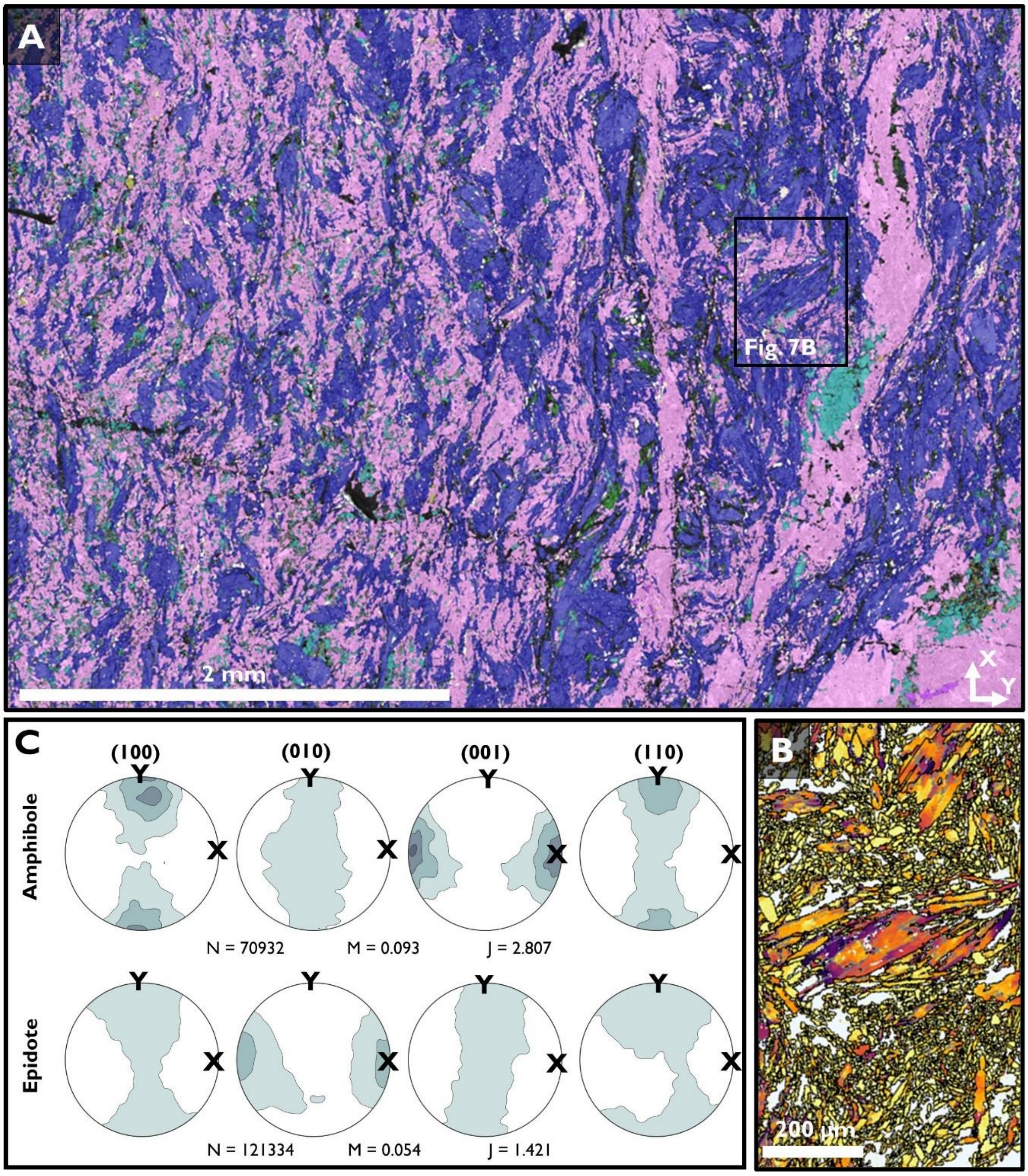

Figure 7 | Microstructural summary of EBSD section AK295. (A) Phase map distributions exhibiting fabric type-A and type-E (see text for explanation). (B) GROD angle map of a close-up showing amphibole and epidote internal misorientations. (C) CPO pole figures of amphibole and epidote from all grains of the EBSD section. For legends, see Fig. 3.

mixed essentially at the grain scale. Locally, smaller bands of (~50 μm thick) aligned epidotes, amphiboles, and albites. Within this fine-grained polyphase foliation, ~0.5 mm sized fractured albite and chlorite porphyroblasts (AK268) or ~1 mm sized euhedral amphibole porphyroblasts (AK222) are oriented at 0 – 10° to the dominant foliation which wraps around these blasts.

Quartz-dominated fabrics (herein called fabric type 'Q' for quartz) contain >80% quartz crystals, are observed in AK222 and AK243 (Figs. 3 and 4) showing mm-to-cm quartz veins in width, together with ~mm sized, sub-to-euhedral albite, calcite, epidote, and amphibole porphyroblasts, and fine-grained and/or inclusions of muscovite, albite, epidote, and amphibole. Quartz in deformed veins consists of a wide range of grain sizes from ~5 μm to > 300 μm in diameter. Quartz exhibits curving and lobate grain boundaries that are locally ameboid, with curved subgrain walls without clear orientations. The veins are parallel to the lineation and consist of crescent-type boudinages with a pinch wavelength of 5 – 15 mm. This fabric type is used for piezometry.

Generally, for all fabric types, grain size decreases with depth in the core (Fig. 2 and S5). For amphiboles and epidotes, this corresponds to grain size change from 22 ± 22 μm to 9 ± 9 μm and 12 ± 8 μm to 7 ± 4 μm, respectively. Sample AK243 deviates from this trend in that epidotes from a recrystallized vein are quite coarse-grained. Moreover, the deepest sample of the core – AK295 – exhibits quite large grain sizes for both amphiboles and epidotes, which may reflect a lithological and/or structural break (cf. Kotowski et al., 2021)(Fig. 2).

Quantitative mineral connectivity analysis

For each fabric type, I assessed the degree of connectivity of the dominant fabric-forming phases (Fig. 8), to quantitatively identify which fabrics comprise load-bearing frameworks and/or interconnected weak layering (cf. Handy, 1994) vs. mixtures of strain-accommodating minerals. The quantitative connectivity procedure of Amiri et al. (2023) shows that amphiboles in type-A and type-AE are always more connected ($C2 > 0.1$ at $r = 100$ px) than epidotes in type-E and type-AE ($C2 < 0.5$ at $r = 100$ px). Amphiboles, therefore, can be treated as load-bearing frameworks, as confirmed by qualitative connectivity images showing large, continuous areas of well-connected amphibole layering throughout the analyzed microstructure. All samples show *C2* and *S2* peaks around 200 – 300 px indicating that amphiboles are connected on ~mm scale. We did not identify any clear differences between amphibole connectivity in amphibole-dominated fabrics (AK278 and AK295) and amphibole connectivity in fabrics containing substantial epidote, albites, and white micas (AK268), indicating that amphibole connectivity is independent of the presence of secondary minerals, at least for the phase distributions analyzed (i.e., up to ~30:70 ratio of amphiboles to secondary phases). Especially in AK278, the connectivity increases at high pixel distances since the amphibole-rich bands are not only connected within a given foliation plane but also locally exhibit amphibole 'bridges' that connect compositional bands across spaced amphibole-defined cleavages. Amphiboles in type-E fabrics typically occur as isolated porphyroblasts or small clusters of grains and do not exhibit strong *C2* connectivity.

Similar to amphibole-rich microstructures, epidote mineral connectivity analysis (Fig. 8) reveals that fabric type-E exhibits well-connected microstructures and can also be treated as an interconnected framework (~0.4 at 100 px). However, epidotes in mixed fabric type-AE, unsurprisingly, are poorly connected (~0 at 100 px), and locally comprise such low proportions of microstructures (e.g., AK268) that they can effectively be ignored when scaling up the microstructural connectivity to macroscopic scales. Furthermore, despite clear epidote connectivity in type-E fabrics (AK278 and AK295), because amphiboles occupy larger volume proportions of the microstructures and a coarser grain size compared to type-E epidotes,

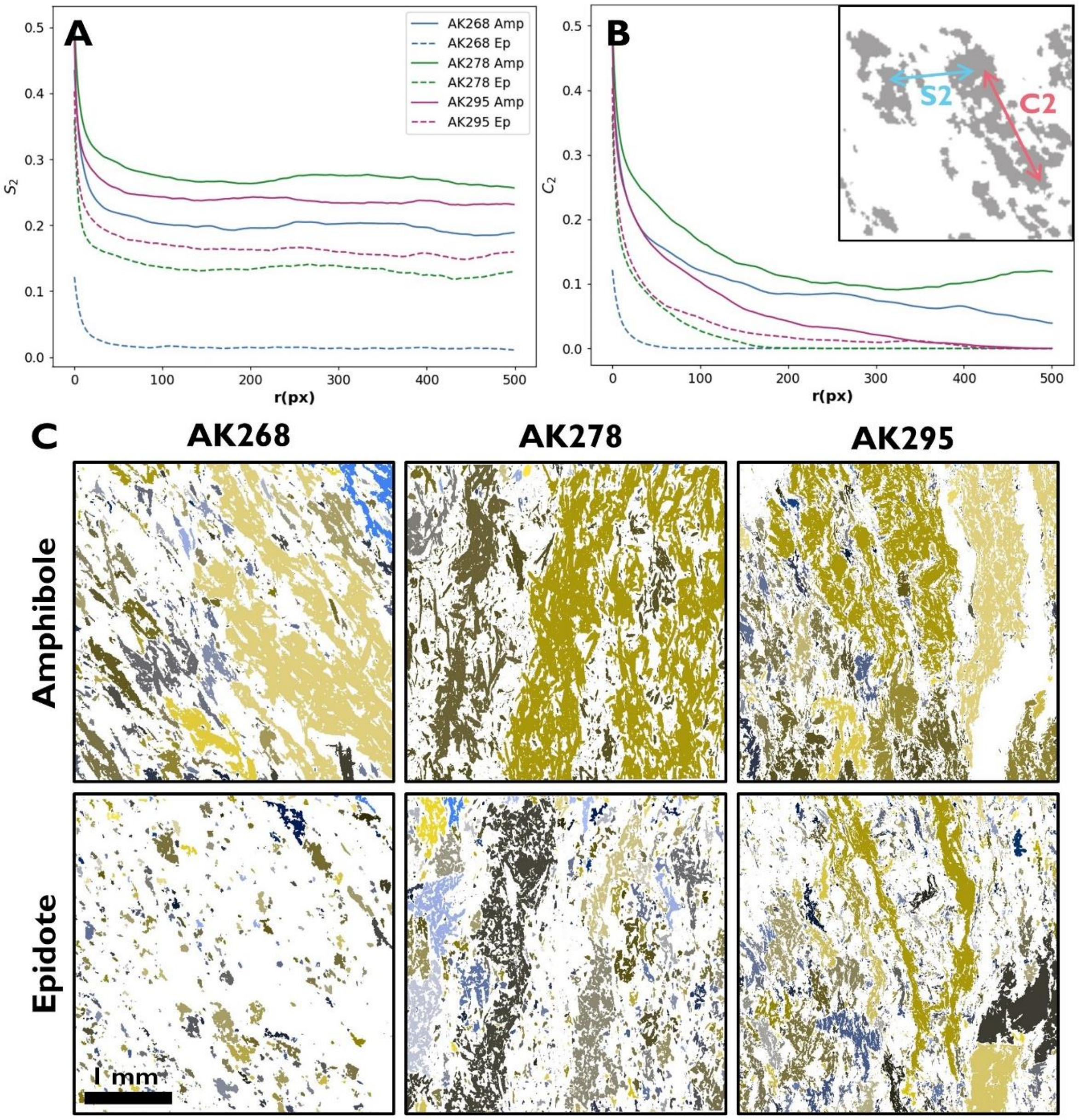

Figure 8 | Summary of connectivity analysis. (A) S2 connectivity analysis showing amphiboles are always more connected than epidotes. (B) C2 connectivity analysis showing as well that amphiboles are always more connected than epidotes. (C) Connectivity maps in which one color represents one interconnected part of amphibole or epidote. All sections have the same scale bar. Note that sample AK268 is type-AE fabric and AK278 and AK295 type-A and type-E fabrics. See Fig. S3 and S4 for more details about connectivity analysis.

therefore amphibole connectivity outweighs the significance of epidote connectivity at the thin section scale. However, recrystallized epidote veins (AK295) form locally well-connected networks through the samples, yielding similar connectivity values (C2 at > 350 px) as amphibole in the same samples. Type-E epidotes show *S2* peaks around ~250 px but these peaks are absent in *C2* plots, which indicates that the epidote-rich compositional bands have similar spacing (~1 mm) from each other, but are not directly connected via epidote bridges across the bands. Epidotes in type-A show similar behavior to epidotes in type-AE and are poorly connected at a range of pixel distances.

4.2. Crystal orientations, grain shapes, and intracrystalline features

Fabric type-A

Amphiboles in fabric type-A consistently exhibit similar bulk CPO patterns across all thin sections indicative of the dominant slip system (hk0)[001] (Figs. 3-7). Poles to (100), (110), and (010) are mostly clustering parallel to the Y direction with some girdling in the YZ plane, indicating that these crystallographic planes are mostly well-aligned within the main shear plane, and locally rotate perpendicular to the shear plane. Regardless of the (hk0) patterns, the [001] always directions show the strongest clustering aligned with the X-direction. Some thin sections exhibit girdles indicative of shear, where the weight-center of the girdle shifts towards the X-direction with depth. M indices stay constant with depth around ~0.1 and J indices decrease with depth from 4.1 at 222 m to 1.0 at 278 m. Rose diagrams of angles between amphibole long-axis orientations and sample average foliation (Fig. S6) demonstrate that amphiboles exhibit consistently strong SPOs with aspect ratios (Fig. S7) that decrease with depth from 3.1 ± 1.7 towards 2.8 ± 0.7.

Amphibole grains exhibit abundant evidence for intracrystalline plasticity, such as patchy grain interiors with gradations of low-angle misorientations, as well as sharp boundaries marking subgrains and tilt walls. Grains with Mean Orientation Spread (MOS), defined as the average internal misorientation, below 2° lack sharp subgrain boundaries, while grains with MOS up to 8° often have subgrain walls (Fig. S8). The MOS increases with increasing grain size from ~1° at ~10 μm to ~2° at ~20 μm (Fig. S9) and decreases slightly with depth from 2.0 ± 1.6° to 0.8 ± 0.9° (Fig. S10). The subgrains are oriented parallel to the long-axes of the amphibole grain and therefore roughly highlight the trace of the foliation, which is different from the predominant trend observed in GROD angle maps of amphiboles, where the primary misorientation tends to be perpendicular to the long-axes (Fig. S8).

Fabric type-E

Epidotes in fabric type-E show weak CPO patterns (Figs. 3 – 7) with the primary slip system (100)[010] and the secondary slip system (001)[010]. Poles to (100), (001), and (110) planes display the strongest clustering parallel to the Y direction with some girdling in the YZ plane, indicating these crystallographic planes are mainly lying within the dominant shear plane, but locally rotate perpendicular to the shear plane. The [010] directions show the strongest clustering aligned with the X direction. The M-indices of epidotes decrease with depth from ~0.06 at 222 m to ~0.03 at 278 m, while the J-indices remain relatively constant at ~1.3. Rose diagrams of angles between epidote long-axis orientations and sample average foliation demonstrate that epidotes exhibit a consistently weak SPO with aspect ratios remaining constant with depth around ~2 (Fig. S6 and S7).

The epidotes display both gradual and sharp increases in misorientation in larger grains, while for smaller grains the MOS is minimal, typically below 1°, and maximum threshold below 6° (Fig S8). Epidotes of ~10 μm in size show MOS < 1°, and do not increase in some samples with increasing grain size but do slightly increase to ~1.5° at ~20 μm locally in type-E fabrics (Fig. S9). The MOS decreases slightly with depth from ~1.1° towards ~0.4° (Fig. S10). Subgrain walls are not clearly aligned with the epidote grain's long axes, nor are they strictly linear, as typically seen in amphiboles; subgrain walls in epidotes exhibit a light subtle curvature (Fig. S8). Locally, grains exhibit a distinctive pattern where two subgrain walls align perpendicularly in the middle of the grain, which results in the subdivision of a grain into four square-shaped subgrains of roughly equal dimensions (Fig. S8).

Fabric type-AE

Amphiboles and epidotes in fabric type-AE (Figs. 3 – 5) show similar bulk CPO in type-A and type-E but have subtle distinctions in clustering and girdling of all planes and directions. Type-AE amphiboles exhibit poles to (010) that show a point maxima parallel to the Z-direction. This CPO geometry is an apparent difference from type-A amphiboles but is only present in one sample. Furthermore, type-AE epidotes have different proportions of operative slip systems, namely (001)[010] as the primary slip system and (100)[010] as a secondary system. With increasing proportion of additional phases (e.g. albite, mica), the J-index increases from 2 to 4 for amphiboles and stays constant around ~1.4 for epidotes. There is no apparent relationship between the proportion to additional phases and M-index. The SPO strength and aspect ratios do not change with increasing proportion of secondary phases. Amphiboles exhibit a mean aspect ratio of ~3, indicating a relatively elongated or rod-like shape while epidotes display a ratio of ~2, suggesting a comparatively more equidimensional slightly brick-like shape (Fig. S6). Both amphibole and epidote show a higher MOS in fabric type-AE, compared to type-A amphiboles and type-E epidotes, with maximum values of 2.0 ± 1.6° and 1.1 ± 1.1° (Fig. S10), respectively. Mean amphibole misorientation spread consistently exceeds that of the epidote mean misorientations by a factor of ~1.5 – 2 times.

Albite and white micas are the most volumetrically abundant additional phases in type-AE fabrics, comprising ~10 – 15% and ~5 – 8% of total mineral content, respectively. Albite exhibits mean grain sizes between 4 – 14 μm, MOS between 0.6 and 1.0°, and very weak or random CPOs (Fig. S11). In some samples, albite pole figures show that the (001) plane is aligned with the X-direction, although it is very weak. Albites commonly show four-grain boundary junctions and straight grain boundaries. White micas exhibit mean grain sizes between 6 – 7 μm, MOS between 1.0 and 1.3°, and also weak CPOs with (100) planes strongly clustered around the Y plane (Fig. S12). White micas intermingle often with albites in bands with epidotes, while amphiboles form their own bands.

Fabric type-Q

Quartz (fabric type-Q) does not exhibit clear CPOs, however, this may partly reflect the low number of grains in the map areas. In the weak CPO patterns, there is some evidence for prism <a> slip in AK222 and non-coaxial rhomb <a> slip and basal <a> slip in AK243 (Fig. S13). Pole figures exhibit strongly clustered planes along X, Y, and Z sample directions, but this probably reflects the low number of relatively large grains in the EBSD maps. This occurs for example in AK222 where A-directions are clustered roughly parallel to the the Z direction, especially seen in $(10\bar{1}0)$ (Fig. S13). The big (~300 μm) grains in this thin section that show lobate and highly interfingering boundaries, contain low misorientation angles (< 3°). Subgrain walls are found in the bigger grains which show dominant orientation of sharp lines within grains, and may be curved but are more or less parallel to each other. In AK243, A-direction pole figures possibly exhibit weak cross girdles in $(10\bar{1}0)$ and $(11\bar{2}0)$ (Fig. S13). The smallest, bulging grains have very low internal misorientations (< 3°), similar to the bigger grains (~300 μm) that have relatively straight grain boundaries and low misorientation angles (< 3°). Subgrain walls are straight and parallel with each other inside one grain, in which they all align roughly at the same distance from each other. Relict grains show very high misorientations (> 8°) around the grain boundaries. The mean MOS is in both thin sections similar: 1.5 ± 1.2°.

4.3. Single grain slip system analysis

Amphiboles in both A- and AE fabric types exhibit multiple slip systems operating in individual grains that are dominated by the easy glide slip system. I analyzed 730 individual amphibole grains between 5 samples (Fig. 9), and 70% of the grains exhibit (hk0)[001] as the primary slip system, with a rotation axis around (010). Subsidiary dislocation is accommodated by the systems (100)[010] and (001)[010] which occur in 12% of the analyzed

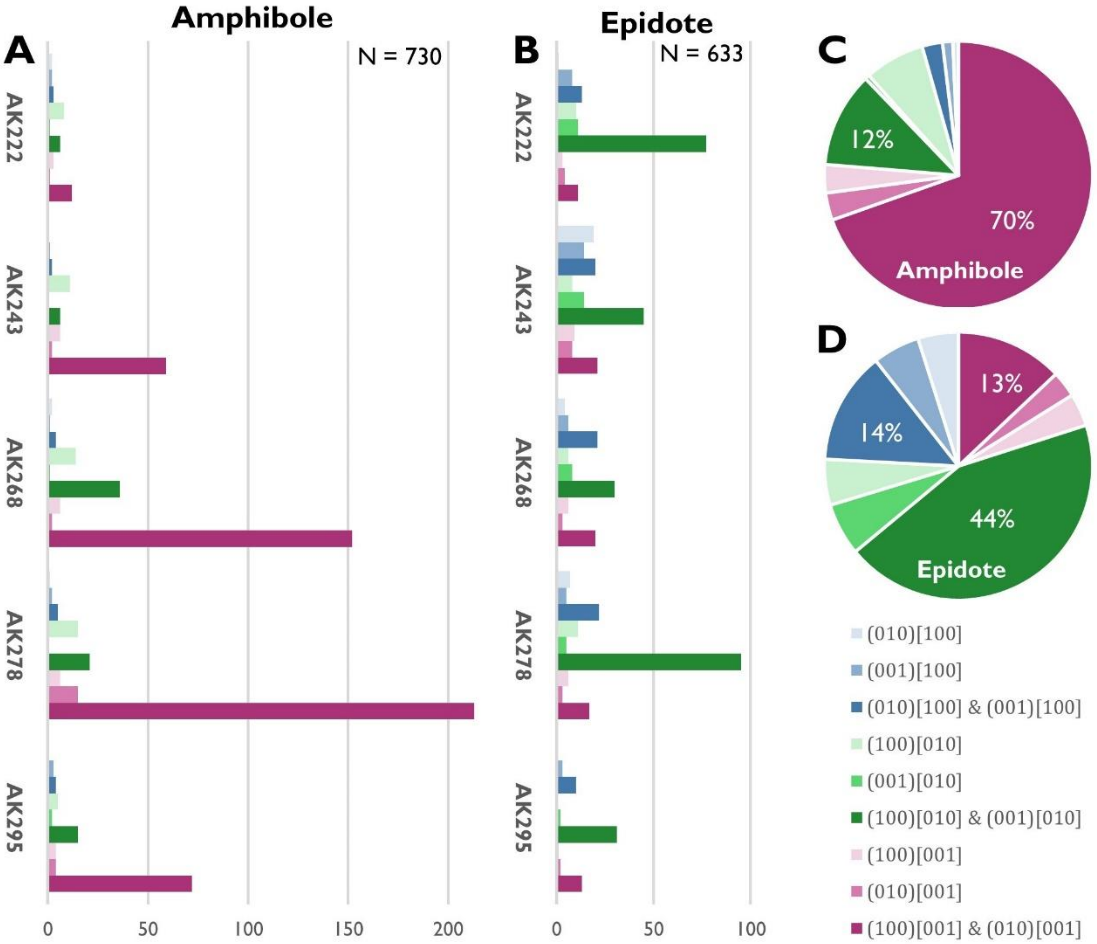

Figure 9 | Summary of single grain analysis. (A) Slip systems of 730 individual amphibole grains. (B) Slip systems of 633 individual epidote grains. (C) Pie chart summary of all amphibole slip systems. (D) Pie chart summary of all epidote slip systems.

grains. Smaller grains tend to exhibit a single slip plane (16% of grains)- whereas larger grains tend to exhibit multiple planes. Subgrain walls that develop parallel to the long-axis of the amphiboles show (hk0)[001] as the clearest slip system, while amphiboles are found as clusters of single grains within interconnected weak layers of epidote, albite, and/or white mica in fabric type-AE or individual, isolated grains within fabric type-E more frequently display (100)[010] and (001)[010] as operative slip systems.

Similar to amphiboles, epidotes locally exhibit multiple slip systems in single grains, with the dominant slip system (100)[010] and (001)[010] for 44% of the analyzed grains (N = 633 grains in 5 samples, Fig. 9). However, a subset of epidote grains in type-E which have SPOs that do not align with the lineation, instead exhibit [100] (24% of grains) and [001] (20% of grains) slip directions. In 30% of the grains, only one apparent slip plane as the main slip system. Subgrain walls perpendicular to epidote long axes show (100)[010] and (001)[010] as the main slip systems. The orientations of epidotes are notably influenced in all fabric types by other mineral phases, particularly albite, and amphibole, resulting in a change from the main slip systems to other directions.

4.4. Quartz vein recrystallized grain size and subgrain piezometry

Recrystallized grain size and subgrain width piezometry analysis (Cross et al., 2017; Goddard et al., 2020) on quartz in deformed veins (fabric type Q) returns 20 – 30 μm for recrystallized grain size and 22 – 33 μm for subgrain width. However, standard deviations for recrystallized grain size are much higher (± 34 – 50) than for subgrain size (± 6 – 8), because recrystallized grains are based on low misorientations which also occur in large grains, while subgrain standard deviations are based on mean subgrain sizes of the lines. Using the Cross et al. (2017), method, we analyzed the mean Grain Orientation Spread taken as a proxy for the presence and density of dislocations to distinguish quantitatively between a subset of fully recrystallized grains and larger, relict, recrystallizing porphyroclasts. The method indicates a recrystallized grain cutoff at internal mean misorientation angles of 2.9 – 3.8° (Fig. S14). Comparing this cutoff to optical and qualitative observations of the recrystallized grain subset, the average grain size of 20 – 30 μm includes mostly small grains but also some larger grains with surprisingly low misorientations. Standard deviations on this method are enormous (± 34 – 50), because of the larger recrystallized grains.

Using the Goddard linear intercept method for walls defined by misorientations between 1 – 10°, we measured mean subgrain sizes on a placed raster with different orientations, resulting in subgrain widths on the order of 22 – 33 c which yield lower stresses than the GOS method and much lower standard deviations (± 6 – 8) in subgrain averages. Subgrain size is slightly larger than the recrystallized grain size, potentially influenced by the presence of larger recrystallized grains with fewer subgrains, elevating the mean value. This method is more straightforward based on measuring subgrain sizes themselves, but is limited in accuracy because it needs to be done by hand (i.e. only ~50 lines have been measured), while the recrystallized method is linked with misorientations, but considers all grains since that is done automatically (i.e. all grains are incorporated). Using the piezometric calibrations of Cross et al. (2017) and Goddard et al. (2020), these grain and subgrain size return flow stresses on the order of 53 – 68 MPa and 13 – 18 MPa, respectively (Fig. 10A), which overlap in calibration error (16 – 375 MPa and 0.15 – 224 MPa).

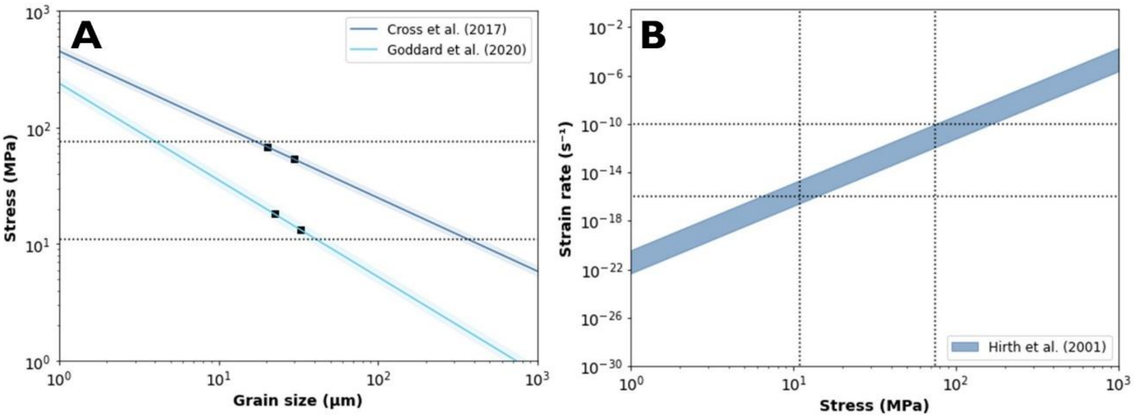

Figure 10 | (A) Results of quartz recrystallized grain size (Cross et al., 2017) and subgrain size (Goddard et al., 2020) piezometry indicating stress estimates of 11 – 75 MPa. (B) Flow law of Hirth et al. (2001) indicating strain rate estimates of 10^{-10} – 10^{-16} s^{-1} based on stress estimates of piezometry. See Fig. S14 for recrystallized grain size piezometry.

5. Discussion

5.1. Interpreted deformation mechanisms operating in epidote-amphibolites

Deformation mechanisms in amphibole-rich, epidote-rich, and polyphase microstructures

Epidote-amphibolites are heterogeneous polyphase rocks that, at the grain scale, exhibit different deformation mechanisms as a function of phase distributions and/or grain size. Herein, I pose interpreted deformation mechanisms for each fabric type outlined above, as a function of the proportions of amphibole and epidote.

Type-A amphiboles show dislocation glide as the dominant deformation mechanism in the LT sole rocks, which locally occurs in conjunction with rigid rotation, and minor dissolution-precipitation creep. Dislocation glide is consistent with pole figures showing the alignment of (100) and (110) planes within the foliation plane and [001] directions parallel to the lineation, and single grain subgrain analysis which indicates dominant operation of the easy dislocation slip system (hk0)[001] (cf. Dollinger and Blacic, 1975). Although this CPO could indicate rigid rotation of amphibole grains since their [001] direction defines the longest crystallographic axes and therefore aligns with the lineation, I consider this mechanism unlikely in samples exhibiting clearly clustered CPOs, due to the prevalence of systematic intracrystalline misorientations (GROS: 0 – 7°) in type-A amphiboles. Furthermore, most samples that record prograde, up-temperature, metamorphic growth zonations (cf. Kotowski et al., 2021) from actinolite to edenite/hornblende (AK268 and AK295) or edenite to pargasite (AK243) reveal progressive increase in average grain misorientation with increasing grain size. This could indicate that metamorphic growth and resultant grain size increase leads to favoring dislocation glide over grain-size sensitive mechanisms, thereby pointing to a mechanism shift from dissolution-creep to dislocation glide with increasing temperature. We emphasize that dislocation glide (i.e., plasticity) operates, but full dynamic recrystallization by dislocation creep appears to be limited since single-grain analyses show that mainly one slip system is operating, and do not indicate that sufficient slip systems are active to accommodate macroscopic ductile flow (cf. van der Wurf, 2023; Wang et al., 2023). Our interpretation of dislocation-mediated deformation is consistent with Elyaszadeh et al. (2018), who presented EBSD data for amphiboles (450 – 650 °C) from Neyriz mantle diapir (Iran) and documented strong CPOs and high GROD angles with systematic alignments of misorientation walls, which they interpreted as evidence for dislocation-mediated deformation. In addition to evidence for dislocation glide and minor DPC, we interpret CPOs characterized by (100), (110), and (010) directions all girdling in the YZ plane, but with strong [001] clustering along the X-direction, to record rigid rotation of amphibole grains. Although these grains also have some internal misorientation indicative of dislocation glide, we distinguish this mechanism based on the fact that the sample with the strongest girdling in the YZ plane also has the lowest average internal misorientations, as is consistent with rigid grain rotation into the shear plane (Kim and Jung, 2019). Therefore, amphiboles in epidote-amphibolites deforming over the temperature window ~400-550˚C exhibit a wide range of mechanisms encompassing rigid rotation and oriented grain growth that may be progressively overprinted by or transition to dislocation glide as grains become favorably oriented in the foliation and grow large enough to prefer intracrystalline plastic mechanisms. Even at maximum temperatures of ~500 – 550 °C, however, recovery mechanisms appear inefficient. Higher temperatures over 600 °C, and/or sufficiently higher pressures in excess of ~1.2 GPa, are apparently required for amphibole to deform by dynamic recrystallization accommodated by dislocation creep, even when amphibole defines a framework-forming aggregate (cf. Skrotzki, 1990; Kotowski and Behr, 2019; Jung et al., 2021; van der Wurf, 2023).

These deformation mechanisms in the LT sole differ from other studies that investigated the HT sole, indicating that not only temperature, mineralogy, and timing conditions are different between the two soles, but also deformation mechanisms. Van der Wurf (2023) investigated the HT metamorphic sole (6 – 12 kbar, 700 – 900 °C) beneath the Mont Albert Ophiolite, Canada, and demonstrated with EBSD that amphiboles (hornblende) are deformed by dislocation creep with subgrain rotation and grain boundary migration both operating simultaneously. Soret et al. (2019) and Agard et al. (2020) studied HT metamorphic soles (~10 kbar, ~850 °C) in the Semail Ophiolite, Oman, and demonstrated with EBSD that amphiboles show brittle deformation, dissolution-precipitation creep and grain boundary sliding as deformation mechanisms.

In contrast to framework-forming type-A amphiboles, type-E framework-forming epidotes exhibit abundant evidence for diffusion-dominated, dissolution-precipitation creep (DPC). This is supported by significantly weaker CPOs in epidotes compared to amphiboles, which we attribute to DPC in crystallographically anisotropic phases, therefore recording preferential dissolution and advection along specific crystal planes and directions, respectively (cf. Fliervoet et al., 1999; Heidelbach et al., 2000; Wassmann and Stöckhert, 2013). Moreover, epidote exhibits a weak to moderate SPO that defines the foliation, comparable to observations from Wassmann and Stöckhert (2013) who interpreted similar fabrics as evidence for DPC in quartz. Epidotes show insignificant or minor increase in grain misorientation with increasing grain size, indicating that grains up to a grain size of at least 30 μm deform dominantly by mechanisms that do *not* impose systematic intracrystalline distortions. Single grain subgrain analysis indicates that multiple slip systems operate in the epidote grains, but that the mean internal misorientations are very small (GROD: ~0.5°), and the suite of apparent slip systems does not necessarily coincide with the weak bulk-rock CPO. The formation of subgrains in epidotes was described by Franz and Liebscher (2008), but they posited that the misorientation may be due to microfracturing. Similarly, Okazaki and Hirth (2020) presented triaxial deformation experiments that indicated semi-brittle behavior in epidotes at similar T conditions as the LT sole rocks described in the present study, but necessarily were done at much faster experimental strain rates than occur in nature. Comparisons of misorientations and band contrast maps convincingly show that intragranular fractures are not present in the epidote-rich layers described in this study. Therefore, we propose that the subtle dislocation microstructures in epidotes are not significant for the dominant phase of deformation recorded in the epidotes, and could reflect a transition to dislocation-based, grain size insensitive mechanisms as grains grow by DPC-processes, or represent weak, low-strain, exhumation-related pulse of dislocations overprinting an earlier, syn-subduction, DPC-related fabric.

Type-AE fabrics, which comprise mixtures of amphibole and epidote alternating with various mixtures of other secondary phases such as albite and white mica, demonstrate unsurprisingly that more strain-accommodating phases complicate the bulk deformation behavior, but amphiboles and epidotes still exhibit their primary dislocation glide and DPC mechanisms, respectively. Based on proportions and types of additional phases, the end-member mechanisms are locally modified. For example, our single-grain subgrain analysis of amphiboles and epidotes in type-AE fabrics tend to exhibit more slip systems, both 'easy' and 'hard' (cf. amphibole: Cao et al., 2010; Elyaszadeh et al., 2018; van der Wurf, 2023; epidote: Park et al., 2020). This may indicate that the slip systems operating are less indicative of a specific deformation mechanism or condition, but rather suggest that slip systems reflect grain-scale stress heterogeneity and whichever slip system is oriented most favorably given a specific grain orientation contained within a weaker load-bearing matrix of albite, mica, quartz, etc. (Handy, 1989, 1994; Lavergne et al., 2013). Furthermore, >40% of these fabrics are composed of other minerals like albite and white mica, and albite exhibits abundant evidence for DPC and grain boundary sliding (GBS) mechanism due to the fine grain size, weak CPOs, and abundant blocky four-grain junctions. White micas also strongly define foliation and form feathery aggregates that may exhibit frictional sliding and/or GBS. When multiple rheologies are active together, phase boundary sliding (GBS sliding between amphibole, epidote, albite, and white mica) may contribute to bulk deformation and substantial weakening, because it accelerates creep rates due to local chemical potential gradients and atomic-scale elemental diffusion (Zhao et al., 2019).

Controls on CPO development in framework-forming phases

My investigations reveal that amphibole and epidote CPO patterns change systematically with depth in the drill core, which appears to reflect changes in factors such as temperature, strain, and the proportions and distributions of phases. Prior research has proposed several different CPOs for amphiboles in nature and experiments that reflect finite strain, temperature, deformation rate, stress, deformation mechanisms and strain geometry (e.g. Hacker and Christie, 1990; Ji et al., 2013; Ko and Jung, 2015). For example, Kim and Jung (2019) categorized amphibole CPO evolution into four types according to a series of deformation experiments: Type-I CPO is common in nature and is characterized by (100) directions normal to the foliation and (001) directions parallel to the lineation (cf. Barruol and Kern, 1996) and forms at low shear strains ($\gamma < 2.1$), low temperatures (<600 °C), moderate to high stresses (~50 – 200 MPa), and under simple shear conditions (Ko and Jung, 2015; Kim and Jung, 2019). Type-I is related to dislocation creep in banded amphibolites (Liu and Cao, 2023). Type-II CPO, which appears to be less common in naturally deformed rocks, is characterized by (100) directions aligned normal to the foliation, and (010) poles aligned parallel to the Z direction (cf. Díaz Aspiroz et al., 2007) under low shear strains ($\gamma < 2.1$), high temperatures (500 – 700 °C), high stresses (>100 MPa) under simple shear experimental conditions (Ko and Jung, 2015; Kim and Jung, 2019). Type III CPO, also rare in nature, is characterized by the alignment of the (100) directions normal to the foliation and the (010) and (001) directions forming a girdle within the foliation plane (cf. Díaz Aspiroz et al., 2007), indicative for high temperature (>600 °C) and low to intermediate stresses (<150 MPa) (Ko and Jung, 2015). Type-III CPO is related to subgrain rotation recrystallization in amphibole porphyroclasts and recrystallized new grains in areas with lower normal stress (Liu and Cao, 2023). Kim and Jung (2019) demonstrated that under moderate-to-high experimental shear strains ($\gamma > 3$), type-IV CPO forms and is characterized by girdles defined by (100) and (110) axes at high-temperature conditions (~500 - 700 °C) and high stresses (~100 – 250 MPa). Type-IV CPO is related to rigid body rotation around the [001] axis of amphibole and grain boundary sliding (GBS) (Liu and Cao, 2023). Therefore, with increasing stress, a CPO switch from type-I to type II occurs; with increasing temperature, a CPO switch from type-I to type-III occurs; and with increasing strain, a CPO switch from type-I to type-IV occurs.

The structurally lowest rocks in the Oman BT1B core samples that contain type-A amphiboles exhibit Type-IV CPOs, while the structurally highest rocks from the dataset show type-I CPO that contain type-AE amphiboles. My observations show a transition from type-I to type-IV with a decreasing proportion of secondary phases such as white mica and albite (Fig. 11) and with increasing depth, and temperature. However, I propose that the (010) axis also features a girdle in type-IV CPO, in contrast to Kim and Jung (2019) but shown by Liu and Cao (2023). Liu and Cao (2023) illustrates a transition from type-I to type-IV, wherein the (010) axis changes from a point maxima along the Z direction to a girdle along the YZ plane, and the (100) directions shift from clustering along the Y-direction and therefore indicative of a well-aligned shear plane, to forming a girdle in the YZ plane with increasing shear strain, while the [001] axis remains unchanged as the direction axis. Amphibole grains in the banded amphibolite are highly elongated by dislocation creep and develop type-I CPO; the fine-grained amphiboles deformed passively by rigid rotation around their [001] axes and grain boundary sliding (GBS) in type-IV CPO (Liu and Cao, 2023). These mechanisms are roughly consistent with our observations that type-A amphiboles show evidence for rigid rotation and dislocation glide (type-IV CPO), and type-AE amphiboles show only dislocation glide (type-I CPO).

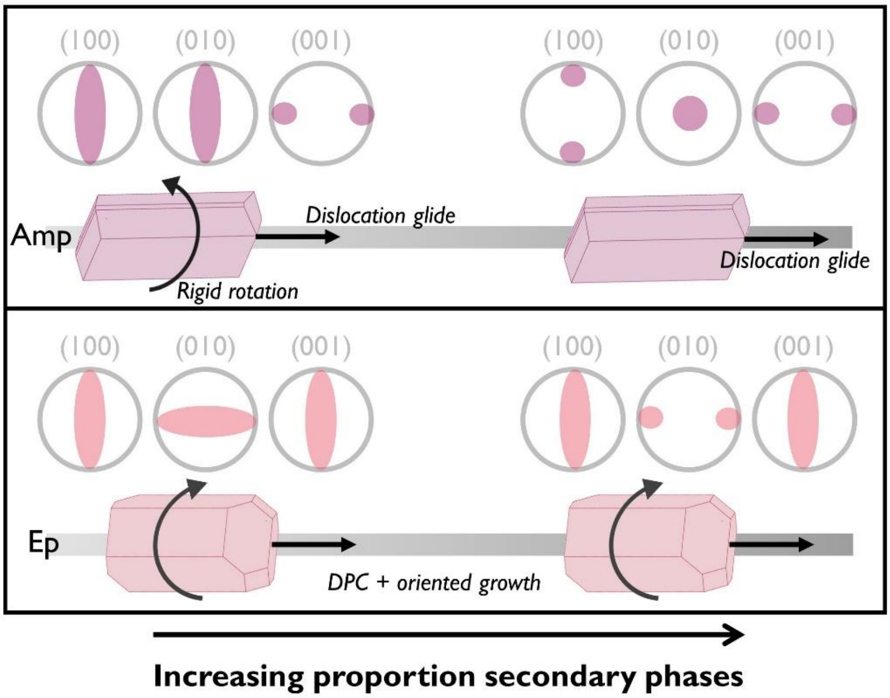

Figure 11 | Synthesis of CPO evolution and deformation mechanisms of amphibole and epidote.

Epidote CPOs in these LT sole rocks are notably different from previous studies that attribute CPO changes to strain magnitude or switches in deformation mechanisms. DPC is not considered to show CPOs in epidotes in previous studies. Park et al. (2020) conducted deformation experiments that demonstrated that under a shear strain of $\gamma = 3$, a type-I epidote CPO develops, characterized by slipping on (100) planes in the [010] direction and reflects the operation of dislocation glide, as demonstrated by Park et al. (2020). Alternative type-I epidote CPO can posit rigid body rotation aligned with the (100) plane, succeeded by deformation parallel to stretching in the [010] direction (Brunsmann et al., 2000). Subsequently, at experimental strains exceeding $\gamma > 4$, type-II CPOs are characterized by (010) planes lying in the shear plane, and [001] directions aligned parallel to flow. Type-II CPO has not yet been reported in naturally deformed rocks, and we do not see evidence for it in epidotes in this study but is attributed to granular flow and diffusion-assisted grain boundary sliding. Recent investigations by De Caroli et al. (2024) reveal very weak epidote CPOs, not similar to the defined type-I and type-II of Park et al. (2020), which they attribute to brittle fracture and incipient dislocation creep.

Table 1. Microstructural summary of amphibole and epidote, linked to deformation mechanisms.

	Amphibole	**Epidote**
Grain shape	Strong, elongated mineral, defines foliation in the metamafic part	Soft, more spherical mineral, defines foliation throughout whole metamorphic sole
Grain size distribution	Bigger grain size than epidote. Larger grain sizes are are not equally distributed	Smaller grain size than amphibole. Equal distribution bigger and smaller grain sizes
Internal misorientation	Bigger orientation spread, subgrains walls and undulose extinction observed	Smaller orientation spread, subgrain walls and undulose extinction in lesser amount observed
CPO	(hk0)[010] primary slip system. Transition of (100), (110), and (010) point maxima to girdles with depth Strong CPO	(100)[010] and (001)[010] primary slip system, but secondary active slip systems are common Weak CPO
SPO	Strong SPO	Weak SPO
Mineral connectivity	Always well connected in every amphibole fabric type	Less connected than amphiboles but still well connected in epidote-rich fabrics, not connected in mixed fabrics.
Interpretation	*Rigid rotation and dislocation glide*	*Dissolution-precipitation creep under differential stress (i.e. oriented grain growth)*

Our CPOs are stronger but consistent with different deformation mechanisms because there is no evidence for brittle behavior for brittle fracture and there are too few misorientations for dislocation creep (Fig. 11). My findings indicate that where epidote exhibits minor dislocation glide, slip occurs along both (100)[010] and (001)[010] slip systems which are most consistent with Park et al.'s (2020) type-I CPOs and therefore suggest that in addition or after DPC (recrystallization) of the grains, plastic strain was imparted to the epidotes, which dominantly occurred along the easiest slip system (type-I) and clearly didn't account for a significant amount of strain.

5.2. Shear zone stress and viscosity estimates

Paleo-flow stress in the LT sole shear zone is constrained through subgrain and recrystallized grain piezometry (Cross et al., 2017; Goddard et al., 2020) which indicate that quartz veins are recrystallized under relatively low-stress conditions, between ~10 – 70 MPa (Fig. 10A). Following arguments by Jessell et al. (2009) we interpret the epidote-amphibolite matrices to exhibit iso-stress to the boudinaged quartz veins, because strain is localized in the heterogeneous matrix material which constitutes a high proportion of the microstructure (>70%), and the weak matrix flows around the harder quartz veins. This is also consistent with Gerbi et al. (2010), in which they modeled the microstructural evolution of rocks comprising the weaker and stronger proportions of an outcrop-scale shear zone, in which their hard phase is similar to our quartz boudins and approximates isostress conditions. Using the stress estimates from piezometry and the Hirth et al. (2001) quartz dislocation creep flow law, we estimate shear zone strain rates on the order of 10^{-10} to 10^{-17} s^{-1} (Fig. 10B). These are consistent with ranges of observed plate boundary strain rates (Bird and Kreemer, 2015) and structural/geologic observations of LT sole thicknesses of 50 – 500 m (Agard et al., 2016) and inferred plate rates of 1 – 10 cm/year from geo/thermochronology on the order 400 – 550 °C (Kotowski et al., 2021; Soret et al., 2022), which return strain rates between $6 \cdot 10^{-11}$ to 10^{-12} s^{-1}.

Constitutive parameters describing the flow behavior of epidote-amphibolite polyphase rheology are poorly constrained, however here we use recent flow laws for amphibole frameworks to provide ballpark quantitative constraints for meta-mafic rock viscosity in warm subduction zones. Available flow laws include dislocation creep of 53% amphibole (hornblende) + 43% plagioclase ($Ab_{70}An_{30}$) by Hacker and Christie (1990), dislocation creep of 58% amphibole (hornblende) + 40% plagioclase ($Ab_{25}An_{75}$) by Wilks and Carter (1990), diffusion creep of albite by Offerhaus et al. (2001), dislocation creep of 80% amphibole (hornblende) + 20% garnet by Wang et al. (2023), and diffusion creep of 55% amphibole (glaucophane) + 30% epidote + 8% quartz + 5% titanite + 2% ilmenite by Tokle et al. (2023). We extrapolate these flow laws over stress-strain rate space for a range of observed grain sizes (10 – 100 μm), and a temperature range of 400 – 550 °C, which encompasses the range of peak temperature experienced during subduction (Kotowski et al., 2021) (Fig. 12). For the strain rates estimated above, and stresses lower than those bracketed by the upper and lower limit from quartz piezometry, the Tokle, Wang, and Offerhaus flow laws return stress estimates within the strain rate window that could capture epidote-amphibolite rheology based on macroscopic strength contrasts. We cautiously present calculations from these flow laws but emphasize that they do not represent the true rheology of these rocks, since these flow laws are derived from different mineral assemblages, phase distributions, and extrapolated from different experimental P-T conditions and strain rates; ultimately, an epidote-amphibolite diffusion creep/DPC flow law is needed for proper quantitative estimates of viscosity.

Stress estimates from piezometry (11 – 75 MPa) and strain rate estimates from Hirth et al. flow (10^{-10} – 10^{-16} s^{-1}) return interface viscosity values of 10^{16} – 10^{23} Pa s. We consider the fast strain rates to be most applicable for the subduction interface at this stage, considering the argument that the heterogeneous shear zones can exhibit isostress conditions, which implies that the deforming epidote-amphibolite matrix must be deforming faster than quartz boudins to explain the observed viscosity contrast. Therefore, faster strain rate estimations from sole thickness and subduction rate yield viscosities on the lower end of the calculated range, between ~10^{16} – 10^{18} Pa-s. These viscosities are lower than previous estimates of subduction interface viscosity for metamorphosed mafic rocks (10^{19} – 10^{21} Pa s) from flow law estimates (Kotowski and Behr, 2019) and seismological models (Billen and Gurnis, 2001; Duarte et al., 2015), but are quite similar to those for different materials like meta-sedimentary rocks (10^{17} – 10^{20} Pa s) (Behr and Becker, 2018).

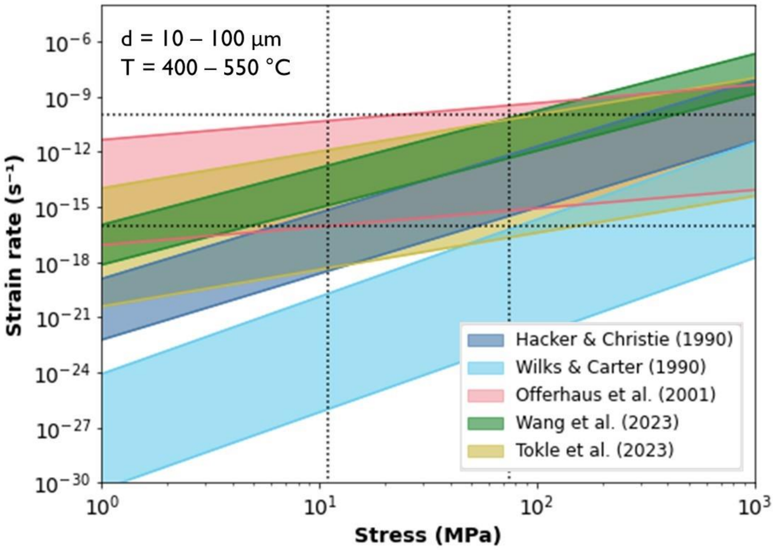

Figure 12 | Flow laws of dislocation creep of amphibole+plagioclase (Hacker and Christie, 1990; Wilks and Carter, 1990), diffusion creep of albite (Offerhaus et al., 2001), dislocation creep of amphibole+garnet (Wang et al., 2023), diffusion creep of epidote+amphibole (Tokle et al., 2023). The stress-strain rate window corresponds to quartz piezometry and flow law calculations (Fig. 10).

6. Implications for subduction dynamics

6.1. Low viscosities at moderate temperatures during subduction infancy

Low interface viscosity has crucial first-order implications on plate-scale dynamics. For example, Behr et al. (2022) showed with numerical modeling of plate interface shear zones that low interface viscosities can lead to mechanical decoupling of the subducting and overriding plates, resulting in relatively short (~10 Myr) timescales of plate velocity increase. Importantly, this effect is independent of slab 'core strength' (defined as the upper viscosity limit within a 12.5-km-thick layer in the center of the subducting lithosphere) and is especially pronounced for slabs that have not yet reached the 660-km discontinuity (Behr et al., 2022). Both plate and trench retreat rates increase with decreasing interface viscosity, whereas higher viscosities (i.e., stronger interface shear zones) lead to lower velocities, steeper slab slopes, and a more vertical slab orientation once the slab reaches the 660-km discontinuity (see also Čížková and Bina, 2013).

In addition to plate velocity and trench kinematics, interface viscosity affects the upper plate stress state. For example, dynamic models by Androvičová et al. (2013) and Gurnis et al. (2004) demonstrate that while high viscosity leads to a neutral or compressive state of stress in the upper plate, lower viscosity and/or stress along the interface triggers upper plate extension and upwelling of hot mantle material into a forearc position. Gurnis et al. (2004) modeled that after subduction initiation, high compressional forces ($3 \cdot 10^{12}$ N/m) are followed by extensional forces ($1 \cdot 10^{12}$ N/m) after 2 Myr in the upper plate. Geologic observations and seismic imaging of subduction initiation at the Puysegur trench, New Zealand, have shown the same evolution of forces, from horizontal compression to vertical extension through time as the initiation process proceeds (Gurnis et al., 2019; Poulaki et al., 2023).

Based on these model constraints, we infer the following dynamic changes to occur as a result of the low viscosity of the epidote-amphibolite interface: lubrication of the plate interface will lead to increased slab sinking velocity, viscous decoupling of the plate boundary and rapid trench rollback, and upper plate extension. In turn, these changes will respectively lead to increased cooling rates or 'refrigeration' of the plate boundary thermal structure, negative buoyancy forces driving self-sustaining subduction, and contemporaneous extrusion of large volumes of mafic igneous rocks in a proto-forearc upper plate configuration – i.e., the future ophiolite lithosphere. In the case of Oman, this rapid succession of events at the inferred switch to self-sustaining subduction is particularly well-constrained in geo/thermochronology of the metamorphic sole (Gnos and Peters, 1993; Hacker, 1994; Hacker et al., 1996; Garber et al., 2020; Kotowski et al., 2021) and the ophiolite crust (Tilton et al., 1981; Warren et al., 2005; Rioux et al., 2012, 2021; Guilmette et al., 2018).

The overlapping ages between epidote-amphibole metamorphism and ophiolite crystallization, and the fact that the interface rheology is so important for plate coupling and subduction velocity (Behr et al., 2022), motivate the connection between epidote-amphibolite LT sole rheology and the transition to self-sustaining subduction. However, during this transition, it is difficult to know exactly what the true trigger is that drives collapse and interface refrigeration. The options are either that refrigeration leads to phase changes that lubricate the interface, *or* that slight cooling finally generates negatively buoyant rocks such as eclogites down-dip of the epidote-amphibolite interface, which leads to collapse, fast advection of cold lithosphere and cooling, and then this stabilization of weak epidote-amphibolites 'locks in' or sustains the plate boundary weakness. Each of these options can be tested in geodynamic models, but either way, the impressive weakness of the 'warm' subduction interface is important as either a physical trigger for slab collapse, or for long-term shear zone maintenance.

6.2. Transient rheology in warm subduction zones

While subduction initiation is based on long-term 'average' or steady-state viscosities, transient rheology implications are on shorter, seismic to decadal, timescales. Polyphase matrix comprises at least two strain-accommodating phases that alternate on the grain-to-mm-to-cm scale and exhibit isostrain behavior, as opposed to isostress behavior between quartz veins and the matrix, because amphibole and epidote are consistent with arguments from Jessell et al. (2009) that hard phases form the load-bearing framework. Different rheological behaviors at the grain-scale will inevitably lead to heterogeneous flow rates and internally stored stress at the grain-scale (Handy, 1989, 1994; Czaplińska et al., 2015). Amphiboles and epidotes exhibit mechanisms that are characterized by different stress and grain size-sensitivities, which may cumulate in a bulk rock exhibiting non-steady state behavior over short (~seconds to decades) timescales (cf. Thom and Kirkpatrick, 2023). Pulses of dislocation glide will lead to internal stress fields by long-range dislocation interactions (Wallis et al., 2022). Especially considering the limited evidence for climb and recovery in minerals exhibiting dislocation-based deformation mechanisms, like amphiboles, deformation to high strains may require transient pulses of plastic deformation to overcome barriers to continued dislocation movement. Both DPC and (climb-limited) dislocation glide are inherently strain-hardening mechanisms since grains grow in the fastest diffusion direction and dislocations tangle, respectively. Therefore, although the long-term composite rheology of epidote-amphibolites may be approximated by that of Newtonian flow in a low-viscosity shear zone, on shorter timescales it must be viewed as a progressive series of transients captured by dissolution and advective flow, dislocation pile-ups and avalanches, and it switches in mechanisms from grain size sensitive to insensitive.

Conceptually, invoking transient creep to describe the flow of polyphase rocks like epidote-amphibolites has implications for possible mechanisms of episodic slow slip and tremor (SST) in subduction zones. However, our interpreted deformation mechanism for epidote DPC leads to grain growth and therefore strain hardening, and for amphibole, dislocation glide leads to tangling and therefore also strain hardening. Both mechanisms need a mechanism switch, fracturing, or pulses of plasticity to continue to create strain, which is required for SST. SST refers to a seismological occurrence detected in many subduction zones, which is marked by swarms of microseismicity, known as tremor, and slipping along the plate interface at rates faster than background plate rates but not fast enough for dynamic failure to release destructive elastic waves (e.g., Rogers and Dragert, 2003). Slow earthquakes occur over a wide range of depth and temperature conditions in subduction zones, commonly spanning 15 – 55 km depths (Kao et al., 2005) and have been precisely relocated to seismically imaged low-velocity layers, interpreted as hydrated meta-stable oceanic crust in the presence of fluids (Shelly et al., 2006; Bostock et al., 2012; Wang et al., 2022). Epidote-amphibolites that record P-T conditions of 7 – 10 kbar, 400 – 550°C (Kotowski et al., 2021) are well situated within known SST depth (e.g., Behr and Bürgmann, 2021; Kirkpatrick et al., 2021). Since the SST mechanism is by definition a non-steady state process, the inference that short timescales of deformation are accommodated by a range of processes exhibiting different rates, grain size-, and stress sensitivities is an attractive conceptual framework for investigating what deformation mechanisms are capable of giving rise to deformation transients, rather than how steady-state flow mechanisms can 'accommodate' fast slip rates (cf. Condit et al., 2022; Thom and Kirkpatrick, 2023).

7. Conclusions

A primary factor driving tectonic plate movement is the subduction of oceanic plates into the lithosphere. Through the subduction lifetime, the temperatures of the metamafic rocks decline resulting in different mineralogy and rheology. Natural subducted rock samples can be taken from metamorphic soles beneath ophiolites, which can help shed light on how subduction operates, especially on subduction initiation. The metamorphic sole, the shear zone of materials from the subducted oceanic slab with the deformed base of the mantle, is comprised of the HT metamorphic sole that forms during the initial stage of underthrusting, and the LT metamorphic sole that forms during the crystallization of the ophiolitic crust. While a lot of work has been done on the rheology of HT metamorphic soles, the LT sole has not yet been investigated in much detail, even though the LT sole is rather important because it captures the transition to self-sustaining subduction.

The LT metamorphic sole formed under P-T conditions of ~7 – 10 kbar, 400 – 550 °C. These metamafic rocks are very fine-grained, strongly foliated and lineated, and commonly exhibit polyphase fabrics in which the hydrous-rich phases amphiboles (~10 – 50 μm), and epidotes (~5 – 20 μm) are key strain-accommodating phases. Building on previous petrologic studies, we selected a suite of 5 samples that record dominantly prograde microstructures through peak epidote-amphibolite facies conditions with minimal retrogressive overprints to characterize the microstructural heterogeneity and interpret operative deformation mechanisms during LT sole subduction. Our Electron Backscattered Diffraction results show that the polyphase epidote-amphibolite fabrics show a combined deformation mechanism of rigid rotation and dislocation glide in amphiboles and dissolution and precipitation creep in epidotes and albites. With increasing content of other minerals, amphiboles retain dominantly dislocation glide microstructures and are well-segregated as well-connected compositional bands across a range of length scales from sub-mm-to-cm. Epidotes, on the other hand, less interconnected than amphiboles, are still connected in epidote-rich fabrics but unconnected in mixed fabrics throughout the microstructures. However, in mixed fabrics, the addition of secondary phases such as albite, also show that diffusion-based deformation mechanisms play an important role, despite the unconnected epidotes in mixed fabrics. We need constitutive constraints on amphibole dislocation glide, and epidote DPC, and the interaction between these two phases, to better quantify the rheology of the LT sole during subduction infancy.

Based on stress estimates from quartz piezometry and strain rate estimates from dislocation creep flow laws (confirmed by independent calculations using inferred ranges of thermochronologically constrained subduction rates and geologically constrained shear zone thicknesses), we calculated that LT sole epidote-amphibolites have low viscosities ($10^{16} – 10^{18}$ Pa s), which are several orders of magnitude lower than previous constraints on a meta-mafic rock viscosity ($10^{19} – 10^{21}$ Pa s). We discuss the significance of such low interface viscosities for subduction plate boundary dynamics, including that it may trigger an increase in the velocity of slab sinking and trench retreat that is a prerequisite for the onset of self-sustaining subduction. Over shorter timescales, since the P-T conditions of these rocks correspond with active subduction shear zones where slow slip and tremor are observed, our microstructural observations provide conceptual frameworks for assessing the likelihood that certain grain-scale mechanisms can give rise to slip transients. Since dislocation glide and dissolution-precipitation creep are both inherently strain hardening mechanisms, and recovery is limited in these rocks due to relatively low temperatures, the rock may need to exhibit semi-cyclic fracturing or pulses of plasticity – i.e., deform by a series of cumulative transients – to deform to high strain.

References

Agard P., Prigent C., Soret M., Dubacq B., Guillot S. and Deldicque D. (2020) Slabitization: Mechanisms controlling subduction development and viscous coupling. *Earth-Science Rev.* **208**, 103259.

Agard P., Yamato P., Soret M., Prigent C., Guillot S., Plunder A., Dubacq B., Chauvet A. and Monié P. (2016) Plate interface rheological switches during subduction infancy: Control on slab penetration and metamorphic sole formation. *Earth Planet. Sci. Lett.* **451**, 208–220.

Ambrose T. K., Waters D. J., Searle M. P., Gopon P. and Forshaw J. B. (2021) Burial, Accretion, and Exhumation of the Metamorphic Sole of the Oman-UAE Ophiolite. *Tectonics* **40**.

Amiri H., Vasconcelos I., Jiao Y., Chen P. E. and Plümper O. (2023) Quantifying microstructures of earth materials using higher-order spatial correlations and deep generative adversarial networks. *Sci. Rep.* **13**, 1–19.

Androvičová A., Čížková H. and van den Berg A. (2013) The effects of rheological decoupling on slab deformation in the Earth's upper mantle. *Stud. Geophys. Geod.* **57**, 460–481.

Bachmann F., Hielscher R. and Schaeben H. (2010) Texture analysis with MTEX- Free and open source software toolbox. *Solid State Phenom.* **160**, 63–68.

Barruol G. and Kern H. (1996) Seismic anisotropy and shear-wave splitting in lower-crustal and upper-mantle rocks from the ivrea zone - Experimental and calculated data. *Phys. Earth Planet. Inter.* **95**, 175–194.

Bechennec F., Le Metour J., Rabu D., Bourdillon-de-Grissac C., de Wever P., Beurrier M. and Villey M. (1990) The Hawasina Nappes: Stratigraphy, palaeogeography and structural evolution of a fragment of the south-Tethyan passive continental margin. *Geol. Soc. Spec. Publ.* **49**, 213–223.

Behr W. M. and Becker T. W. (2018) Sediment control on subduction plate speeds. *Earth Planet. Sci. Lett.* **502**, 166–173.

Behr W. M. and Bürgmann R. (2021) *What's down there? The structures, materials and environment of deep-seated slow slip and tremor.*,

Behr W. M., Holt A. F., Becker T. W. and Faccenna C. (2022) The effects of plate interface rheology on subduction kinematics and dynamics. *Geophys. J. Int.* **230**, 796–812.

Behr W. M. and Platt J. P. (2011) A naturally constrained stress profile through the middle crust in an extensional terrane. *Earth Planet. Sci. Lett.* **303**, 181–192.

Belgrano T. M., Diamond L. W., Vogt Y., Biedermann A. R., Gilgen S. A. and Al-Tobi K. (2019) A revised map of volcanic units in the Oman ophiolite: Insights into the architecture of an oceanic proto-arc volcanic sequence. *Solid Earth* **10**, 1181–1217.

Bercovici D. (2003) The generation of plate tectonics from mantle convection. *Earth Planet. Sci. Lett.* **205**, 107–121.

Bercovici D. and Ricard Y. (2012) Mechanisms for the generation of plate tectonics by two-phase grain-damage and pinning. *Phys. Earth Planet. Inter.* **202–203**, 27–55.

Billen M. I. and Gurnis M. (2001) A low viscosity wedge in subduction zones. *Earth Planet. Sci. Lett.* **193**, 227–236.

Bird P. and Kreemer C. (2015) Revised tectonic forecast of global shallow seismicity based on version 2.1 of the global strain rate map. *Bull. Seismol. Soc. Am.* **105**, 152–166.

Bostock M. G., Royer A. A., Hearn E. H. and Peacock S. M. (2012) Low frequency earthquakes below southern Vancouver Island. *Geochemistry, Geophys. Geosystems* **13**, 1–12.

Brodie K. H. and Rutter E. H. (1985) On the relationship between deformation and metamorphism, with special reference to the behavior of basic rocks. *Metamorph. React. Kinet. Textures, Deform.*, 138–179.

Brunsmann A., Franz G., Erzinger J. and Landwehr D. (2000) Zoisite- and clinozoisite-segregations in metabasites (Tauern Window, Austria) as evidence for high-pressure fluid-rock interaction. *J. Metamorph. Geol.* **18**, 1–21.

Cao S., Liu J. and Leiss B. (2010) Orientation-related deformation mechanisms of naturally deformed amphibole in amphibolite mylonites from the Diancang Shan, SW Yunnan, China. *J. Struct. Geol.* **32**, 606–622.

De Caroli S., Fagereng Å., Ujiie K., Blenkinsop T., Meneghini F. and Muir D. (2024) Deformation microstructures of low- and high-strain epidote-blueschist (Ryukyu arc, Japan): Implications for subduction interface rheology. *J. Struct. Geol.* **180**, 1–14.

Chauvet F., Lapierre H., Maury R. C., Bosch D., Basile C., Cotten J., Brunet P. and Campillo S. (2011) Triassic alkaline magmatism of the Hawasina Nappes: Post-breakup melting of the Oman lithospheric mantle modified by the Permian Neotethyan Plume. *Lithos* **122**, 122–136.

Chen H., He X., Teng Q., Sheriff R. E., Feng J. and Xiong S. (2020) Super-resolution of real-world rock microcomputed tomography images using cycle-consistent generative adversarial networks. *Phys. Rev. E* **101**.

Čížková H. and Bina C. R. (2013) Effects of mantle and subduction-interface rheologies on slab stagnation and trench rollback. *Earth Planet. Sci. Lett.* **379**, 95–103.

Cloetingh S. A. P. L., Tankard A. J., Welsink H. and Jenkins H. (1989) On the initiation of subduction zones. *Pure Appl. Geophys.*, 7–29.

Coleman R. G. (1981) Tectonic Setting for Ophiolite Obduction in Oman. *J. Geophys. Res.* **86**, 2497–2508.

Condit C. B., French M. E., Hayles J. A., Yeung L. Y., Chin E. J. and Lee C. T. A. (2022) Rheology of Metasedimentary Rocks at the Base of the Subduction Seismogenic Zone. *Geochemistry, Geophys. Geosystems* **23**, 1–32.

Cowan R. J., Searle M. P. and Waters D. J. (2014) Structure of the metamorphic sole to the Oman Ophiolite, Sumeini Window and Wadi Tayyin: Implications for ophiolite obduction processes. *Geol. Soc. Spec. Publ.* **392**, 155–175.

Cross A. J., Prior D. J., Stipp M. and Kidder S. (2017) The recrystallized grain size piezometer for quartz: An EBSD-based calibration. *Geophys. Res. Lett.* **44**, 6667–6674.

Czaplińska D., Piazolo S. and Zibra I. (2015) The influence of phase and grain size distribution on the dynamics of strain localization in polymineralic rocks. *J. Struct. Geol.* **72**, 15–32.

Díaz Aspiroz M., Lloyd G. E. and Fernández C. (2007) Development of lattice preferred orientation in clinoamphiboles deformed under low-pressure metamorphic conditions. A SEM/EBSD study of metabasites from the Aracena metamorphic belt (SW Spain). *J. Struct. Geol.* **29**, 629–645.

Dollinger G. and Blacic J. D. (1975) Deformation mechanisms in experimentally and naturally deformed amphiboles. *Earth Planet. Sci. Lett.* **26**, 409–416.

van Driel S. (2023) Peak Pressure-Temperature of the Low- Temperature metamorphic sole beneath the Semail ophiolite (Oman) from thermodynamic models. Utrecht University.

Duarte J. C., Schellart W. P. and Cruden A. R. (2015) How weak is the subduction zone interface?

Geophys. Res. Lett. **42**, 2664–2673.

Elyaszadeh R., Prior D. J., Sarkarinejad K. and Mansouri H. (2018) Different slip systems controlling crystallographic preferred orientation and intracrystalline deformation of amphibole in mylonites from the Neyriz mantle diapir, Iran. *J. Struct. Geol.* **107**, 38–52.

Faul U. (2021) Dislocation structure of deformed olivine single crystals from conventional EBSD maps. *Phys. Chem. Miner.* **48**, 1–15.

Fliervoet T. F., Drury M. R. and Chopra P. N. (1999) Crystallographic preferred orientations and misorientations in some olivine rocks deformed by diffusion or dislocation creep. *Tectonophysics* **303**, 1–27.

Franz G. and Liebscher A. (2008) Physical and chemical properties of the Epidote Minerals - An Introduction. *Rev. Mineral. Geochemistry* **56**, 1–82.

Garber J. M., Rioux M., Kylander-Clark A. R. C., Hacker B. R., Vervoort J. D. and Searle M. P. (2020) Petrochronology of Wadi Tayin Metamorphic Sole Metasediment, With Implications for the Thermal and Tectonic Evolution of the Samail Ophiolite (Oman/UAE). *Tectonics* **39**.

Gerbi C., Culshaw N. and Marsh J. (2010) Magnitude of weakening during crustal-scale shear zone development. *J. Struct. Geol.* **32**, 107–117.

Gerya T. (2022) Numerical modeling of subduction: State of the art and future directions. *Geosphere* **18**, 503–561.

Gerya T. V., Connolly J. A. D. and Yuen D. A. (2008) Why is terrestrial subduction one-sided? *Geology* **36**, 43–46.

Getsinger A. J., Hirth G., Stünitz H. and Goergen E. T. (2013) Influence of water on rheology and strain localization in the lower continental crust. *Geochemistry, Geophys. Geosystems* **14**, 2247–2264.

Gnos E. and Peters T. (1993) Contributions to Mineralogy and Petrology K-Ar ages of the metamorphic sole of the Semail Ophiolite: implications for ophiolite cooling history. *Contrib Miner. Pet.* **1**, 325–332.

Godard M., Carter E. J., Decrausaz T., Lafay R., Bennett E., Kourim F., de Obeso J. C., Michibayashi K., Harris M., Coggon J. A., Teagle D. A. H. and Kelemen P. B. (2021) Geochemical Profiles Across the Listvenite-Metamorphic Transition in the Basal Megathrust of the Semail Ophiolite: Results From Drilling at OmanDP Hole BT1B. *J. Geophys. Res. Solid Earth* **126**.

Goddard R. M., Hansen L. N., Wallis D., Stipp M., Holyoke C. W., Kumamoto K. M. and Kohlstedt D. L. (2020) A Subgrain-Size Piezometer Calibrated for EBSD. *Geophys. Res. Lett.* **47**.

Goodenough K. M., Styles M. T., Schofield D., Thomas R. J., Crowley Q. C., Lilly R. M., McKervey J., Stephenson D. and Carney J. N. (2010) Architecture of the Oman-UAE ophiolite: Evidence for a multi-phase magmatic history. *Arab. J. Geosci.* **3**, 439–458.

Guilmette C., Smit M. A., van Hinsbergen D. J. J., Gürer D., Corfu F., Charette B., Maffione M., Rabeau O. and Savard D. (2018) Forced subduction initiation recorded in the sole and crust of the Semail Ophiolite of Oman. *Nat. Geosci.* **11**, 688–695.

Gurnis M., Van Avendonk H., Gulick S. P. S., Stock J., Sutherland R., Hightower E., Shuck B., Patel J., Williams E., Kardell D., Herzig E., Idini B., Graham K., Estep J. and Carrington L. (2019) Incipient subduction at the contact with stretched continental crust: The Puysegur Trench. *Earth Planet. Sci. Lett.* **520**, 212–219.

Gurnis M., Hall C. and Lavier L. (2004) Evolving force balance during incipient subduction.

Geochemistry, Geophys. Geosystems **5**.

Hacker B. R. (1994) Rapid Emplacement of Young Oceanic Lithosphere: Argon Geochronology of the Oman Ophiolite. *Science (80-.).* **265**, 1563–1565.

Hacker B. R. and Christie J. M. (1990) Experimentally Deformed and Metamorphosed Amphibolite. *Geophys. Monogr. Ser.* **56**, 127–147.

Hacker B. R., Mosenfelder J. L. and Gnos E. (1996) Rapid emplacement of the Oman ophiolite: Thermal and geochronologic constraints. *Tectonics* **15**, 1230–1247.

Hamers M. F., Niemeijer A. R. and Drury M. R. (2023) Cathodoluminescence as a tracing technique for quartz precipitation in low velocity shear experiments. *Sci. Rep.* **13**, 1–16.

Handy M. R. (1989) Deformation regimes and the rheological evolution of fault zones in the lithosphere: the effects of pressure, temperature, grainsize and time. *Tectonophysics* **163**, 119–152.

Handy M. R. (1994) Flow laws for rocks containing two non-linear viscous phases: A phenomenological approach. *J. Struct. Geol.* **16**, 287–301.

Hansen V. L. (2007) Subduction origin on early Earth: A hypothesis. *Geology* **35**, 1059–1062.

Heidelbach F., Post A. and Tullis J. (2000) Crystallographic preferred orientation in albite samples deformed experimentally by dislocation and solution precipitation creep. *J. Struct. Geol.* **22**, 1649–1661.

Hirth G., Teyssier C. and Dunlap W. J. (2001) An evaluation of quartzite flow laws based on comparisons between experimentally and naturally deformed rocks. *Int. J. Earth Sci.* **90**, 77–87.

Holyoke C. W. and Kronenberg A. K. (2010) Accurate differential stress measurement using the molten salt cell and solid salt assemblies in the Griggs apparatus with applications to strength, piezometers and rheology. *Tectonophysics* **494**, 17–31.

Humphreys F. J., Bate P. S. and Hurley P. J. (2001) Orientation averaging of electron backscattered diffraction data. *J. Microsc.* **201**, 50–58.

Jessell M. W., Bons P. D., Griera A., Evans L. A. and Wilson C. J. L. (2009) A tale of two viscosities. *J. Struct. Geol.* **31**, 719–736.

Ji S., Shao T., Michibayashi K., Long C., Wang Q., Kondo Y., Zhao W., Wang H. and Salisbury M. H. (2013) A new calibration of seismic velocities, anisotropy, fabrics, and elastic moduli of amphibole-rich rocks. *J. Geophys. Res. Planets* **118**, 4699–4728.

Jiao Y., Stillinger F. H. and Torquato S. (2008) Modeling heterogeneous materials via two-point correlation functions. II. Algorithmic details and applications. *Phys. Rev. E - Stat. Nonlinear, Soft Matter Phys.* **77**, 1–35.

Jordan P. (1988) The rheology of polymineralic rocks - an approach. *Geol. Rundschau* **77**, 285–294.

Jung S., Yamamoto T., Ando J. I. and Jung H. (2021) Dislocation creep of olivine and amphibole in amphibole peridotites from Åheim, norway. *Minerals* **11**.

Kao H., Shan S. J., Dragert H., Rogers G., Cassidy J. F. and Ramachandran K. (2005) A wide depth distribution of seismic tremors along the northern Cascadia margin. *Nature* **436**, 841–844.

Kemp D. V. and Stevenson D. J. (1996) A tensile, flexural model for the initiation of subduction. *Geophys. J. Int.* **125**, 73–93.

Kim J. and Jung H. (2019) New Crystal Preferred Orientation of Amphibole Experimentally Found in

Simple Shear. *Geophys. Res. Lett.* **46**, 12996–13005.

Ko B. and Jung H. (2015) Crystal preferred orientation of an amphibole experimentally deformed by simple shear. *Nat. Commun.* **6**.

Kotowski A. J. and Behr W. M. (2019) Length scales and types of heterogeneities along the deep subduction interface: Insights from exhumed rocks on Syros Island, Greece. *Geosphere* **15**, 1038–1065.

Kotowski A. J., Cloos M., Stockli D. F. and Bos Orent E. (2021) Structural and Thermal Evolution of an Infant Subduction Shear Zone: Insights From Sub-Ophiolite Metamorphic Rocks Recovered From Oman Drilling Project Site BT-1B. *J. Geophys. Res. Solid Earth* **126**.

Lavergne F., Brenner R. and Sab K. (2013) Effects of grain size distribution and stress heterogeneity on yield stress of polycrystals: A numerical approach. *Comput. Mater. Sci.* **77**, 387–398.

Legland D., Arganda-Carreras I. and Andrey P. (2016) MorphoLibJ: Integrated library and plugins for mathematical morphology with ImageJ. *Bioinformatics* **32**, 3532–3534.

Li Y. and Gurnis M. (2023) A simple force balance model of subduction initiation. *Geophys. J. Int.* **232**, 128–146.

Liu J. and Cao S. (2023) Development of Amphibole Crystal Preferred Orientations (CPOs) and Their Effects on Seismic Anisotropy in Deformed Amphibolites. *J. Geophys. Res. Solid Earth* **128**, 1–24.

Lopez-Sanchez M. A. (2020) Which average, how many grains, and how to estimate robust confidence intervals in unimodal grain size populations. *J. Struct. Geol.* **135**.

MacLeod C. J., Johan Lissenberg C. and Bibby L. E. (2013) "Moist MORB" axial magmatism in the Oman ophiolite: The evidence against a mid-ocean ridge origin. *Geology* **41**, 459–462.

Mainprice D., Bachmann F., Hielscher R. and Schaeben H. (2015) Descriptive tools for the analysis of texture projects with large datasets using MTEX: Strength, symmetry and components. *Geol. Soc. Spec. Publ.* **409**, 251–271.

Menzel M. D., Urai J. L., de Obeso J. C., Kotowski A., Manning C. E., Kelemen P. B., Kettermann M., Jesus A. P. and Harigane Y. (2020) Brittle Deformation of Carbonated Peridotite—Insights From Listvenites of the Samail Ophiolite (Oman Drilling Project Hole BT1B). *J. Geophys. Res. Solid Earth* **125**.

Mueller S. and Phillips R. J. (1991) On The Initiation of Subduction. *J. Geophys. Res.* **96**, 651–665.

Nicolas A., Boudier F. and Ildefonse B. (1996) Variable crustal thickness in the Oman ophiolite: Implication for oceanic crust. *J. Geophys. Res. Solid Earth* **101**, 17941–17950.

Nicolas A., Reuber I. and Benn K. (1988) A new magma chamber model based on structural studies in the Oman ophiolite. *Tectonophysics* **151**, 87–105.

de Obeso J. C. and Kelemen P. B. (2018) Fluid rock interactions on residual mantle peridotites overlain by shallow oceanic limestones: Insights from Wadi Fins, Sultanate of Oman. *Chem. Geol.* **498**, 139–149.

Offerhaus L. J., Wirth R. and Dresen G. (2001) High-temperature creep of polycrystalline albite. *Deform. Mech. Rheol. Tectonics* **124**, 107.

Okazaki K. and Hirth G. (2020) Deformation of mafic schists from subducted oceanic crust at high pressure and temperature conditions. *Tectonophysics* **774**, 228217.

Park Y., Jung S. and Jung H. (2020) Lattice preferred orientation and deformation microstructures of glaucophane and epidote in experimentally deformed epidote blueschist at high pressure. *Minerals* **10**, 1–21.

Pearce M. A., Wheeler J. and Prior D. J. (2011) Relative strength of mafic and felsic rocks during amphibolite facies metamorphism and deformation. *J. Struct. Geol.* **33**, 662–675.

Poulaki E. M., Stockli D. F. and Shuck B. D. (2023) Pre-Subduction Architecture Controls Coherent Underplating During Subduction and Exhumation (Nevado-Filábride Complex, Southern Spain). *Geochemistry, Geophys. Geosystems* **24**.

Regenauer-Lieb K., Yuen D. A. and Branlund J. (2001) The initiation of subduction: Criticality by addition of water? *Science (80-.).* **294**, 578–580.

Rioux M., Benoit M., Amri I., Ceuleneer G., Garber J. M., Searle M. and Leal K. (2021) The Origin of Felsic Intrusions Within the Mantle Section of the Samail Ophiolite: Geochemical Evidence for Three Distinct Mixing and Fractionation Trends. *J. Geophys. Res. Solid Earth* **126**, 1–26.

Rioux M., Bowring S., Kelemen P., Gordon S., Dudás F. and Miller R. (2012) Rapid crustal accretion and magma assimilation in the Oman-U.A.E. ophiolite: High precision U-Pb zircon geochronology of the gabbroic crust. *J. Geophys. Res. Solid Earth* **117**.

Rioux M., Garber J., Bauer A., Bowring S., Searle M., Kelemen P. and Hacker B. (2016) Synchronous formation of the metamorphic sole and igneous crust of the Semail ophiolite: New constraints on the tectonic evolution during ophiolite formation from high-precision U–Pb zircon geochronology. *Earth Planet. Sci. Lett.* **451**, 185–195.

Rioux M., Garber J. M., Searle M., Crowley J. L., Stevens S., Schmitz M., Kylander-Clark A., Leal K., Ambrose T. and Smye A. J. (2023) The temporal evolution of subduction initiation in the Samail ophiolite: High-precision U–Pb zircon petrochronology of the metamorphic sole. *J. Metamorph. Geol.* **41**, 817–847.

Rogers G. and Dragert H. (2003) Episodic tremor and slip on the Cascadia subduction zone: The chatter of silent slip. *Science (80-.).* **300**, 1942–1943.

Searle M. P. and Cox J. (2002) Subduction zone metamorphism during formation and emplacement of the Semail ophiolite in the Oman Mountains. *Geol. Mag.* **139**, 241–255.

Searle M. P., Waters D. J., Martin H. N. and Rex D. C. (1994) Structure and metamorphism of blueschist-eclogite facies rocks from the northeastern Oman Mountains. *J. - Geol. Soc.* **151**, 555–576.

Sheehan N. and Torquato S. (2001) Generating microstructures with specified correlation functions. *J. Appl. Phys.* **89**, 53–60.

Shelly D. R., Beroza G. C., Ide S. and Nakamula S. (2006) Low-frequency earthquakes in Shikoku, Japan, and their relationship to episodic tremor and slip. *Nature* **442**, 188–191.

Shuck B., Gulick S. P. S., Van Avendonk H. J. A., Gurnis M., Sutherland R., Stock J. and Hightower E. (2022) Stress transition from horizontal to vertical forces during subduction initiation. *Nat. Geosci.* **15**, 149–155.

Skemer P., Katayama I., Jiang Z. and Karato S. I. (2005) The misorientation index: Development of a new method for calculating the strength of lattice-preferred orientation. *Tectonophysics* **411**, 157–167.

Skrotzki W. (1990) Microstructure in hornblende of a mylonitic amphibolite. *Geol. Soc. Spec. Publ.* **54**, 321–325.

Soret M., Agard P., Dubacq B., Plunder A. and Yamato P. (2017) Petrological evidence for stepwise accretion of metamorphic soles during subduction infancy (Semail ophiolite, Oman and UAE). *J.*

Metamorph. Geol. **35**, 1051–1080.

Soret M., Agard P., Ildefonse B., Dubacq B., Prigent C. and Rosenberg C. (2019) Deformation mechanisms in mafic amphibolites and granulites: Record from the Semail metamorphic sole during subduction infancy. *Solid Earth* **10**, 1733–1755.

Soret M., Bonnet G., Agard P., Larson K. P., Cottle J. M., Dubacq B., Kylander-Clark A. R. C., Button M. and Rividi N. (2022) Timescales of subduction initiation and evolution of subduction thermal regimes. *Earth Planet. Sci. Lett.* **584**, 117521.

Stern R. J. (2004) Subduction initiation: Spontaneous and induced. *Earth Planet. Sci. Lett.* **226**, 275–292.

Stern R. J. and Gerya T. (2018) Subduction initiation in nature and models: A review. *Tectonophysics* **746**, 173–198.

Stipp M. and Tullis J. (2003) The recrystallized grain size piezometer for quartz. *Geophys. Res. Lett.* **30**, 1–5.

Stokes M. R., Wintsch R. P. and Southworth C. S. (2012) Deformation of amphibolites via dissolution-precipitation creep in the middle and lower crust. *J. Metamorph. Geol.* **30**, 723–737.

Tharp T. M. (1985) Numerical models of subduction and forearc deformation. *Geophys. J. R. Astron. Soc.* **80**, 419–437.

Thom C. A. and Kirkpatrick J. D. (2023) A mechanism for transient creep in crustal shear zones. *Geology* **51**, 642–646.

Tilton G. R., Hopson C. A. and Wright J. E. (1981) Uranium-lead isotopic ages of the Samail ophiolite, Oman, with applications to Tethyan ocean ridge tectonics. *J. Geophys. Res.* **86**, 2763–2775.

Tokle L., Hufford L. J., Behr W. M., Morales L. F. G. and Madonna C. (2023) Diffusion Creep of Sodic Amphibole-Bearing Blueschist Limited by Microboudinage. *J. Geophys. Res. Solid Earth* **128**.

Ueda K., Gerya T. and Sobolev S. V. (2008) Subduction initiation by thermal-chemical plumes: Numerical studies. *Phys. Earth Planet. Inter.* **171**, 296–312.

Wallis D., Sep M. and Hansen L. N. (2022) Transient Creep in Subduction Zones by Long-Range Dislocation Interactions in Olivine. *J. Geophys. Res. Solid Earth* **127**.

Wang W., Savage M. K., Yates A., Zal H. J., Webb S., Boulton C., Warren-Smith E., Madley M., Stern T., Fry B., Mochizuki K. and Wallace L. (2022) Temporal velocity variations in the northern Hikurangi margin and the relation to slow slip. *Earth Planet. Sci. Lett.* **584**, 117443.

Wang X., Zhang J. F., Tommasi A., Lopez-Sanchez M. A., Jing Z. C., Shi F., Liu W. L. and Barou F. (2023) Experimental Evidence for a Weak Calcic-Amphibole-Rich Deep Crust in Orogens. *Geophys. Res. Lett.* **50**, 1–12.

Wang X., Zhang J., Tommasi A., Jing Z. and Yuan M. (2021) Microstructure and seismic properties of amphibole-rich rocks from the deep crust in southern Tibet. *Tectonophysics* **811**.

Warren C. J., Parrish R. R., Waters D. J. and Searle M. P. (2005) Dating the geologic history of Oman's Semail ophiolite: Insights from U-Pb geochronology. *Contrib. to Mineral. Petrol.* **150**, 403–422.

Warren J. M. and Hirth G. (2006) Grain size sensitive deformation mechanisms in naturally deformed peridotites. *Earth Planet. Sci. Lett.* **248**, 438–450.

Wassmann S. and Stöckhert B. (2013) Rheology of the plate interface - Dissolution precipitation creep in high pressure metamorphic rocks. *Tectonophysics* **608**, 1–29.

Wilks K. R. and Carter N. L. (1990) Rheology of some continental lower crustal rocks. *Tectonophysics* **182**, 57–77.

van der Wurf T. (2023) Effects of thermal structure and amphibole deformation mechanisms on the rheology of a proto-plate interface during incipient subduction. Utrecht University.

Zhao N., Hirth G., Cooper R. F., Kruckenberg S. C. and Cukjati J. (2019) Low viscosity of mantle rocks linked to phase boundary sliding. *Earth Planet. Sci. Lett.* **517**, 83–94.

Supplementary Figures

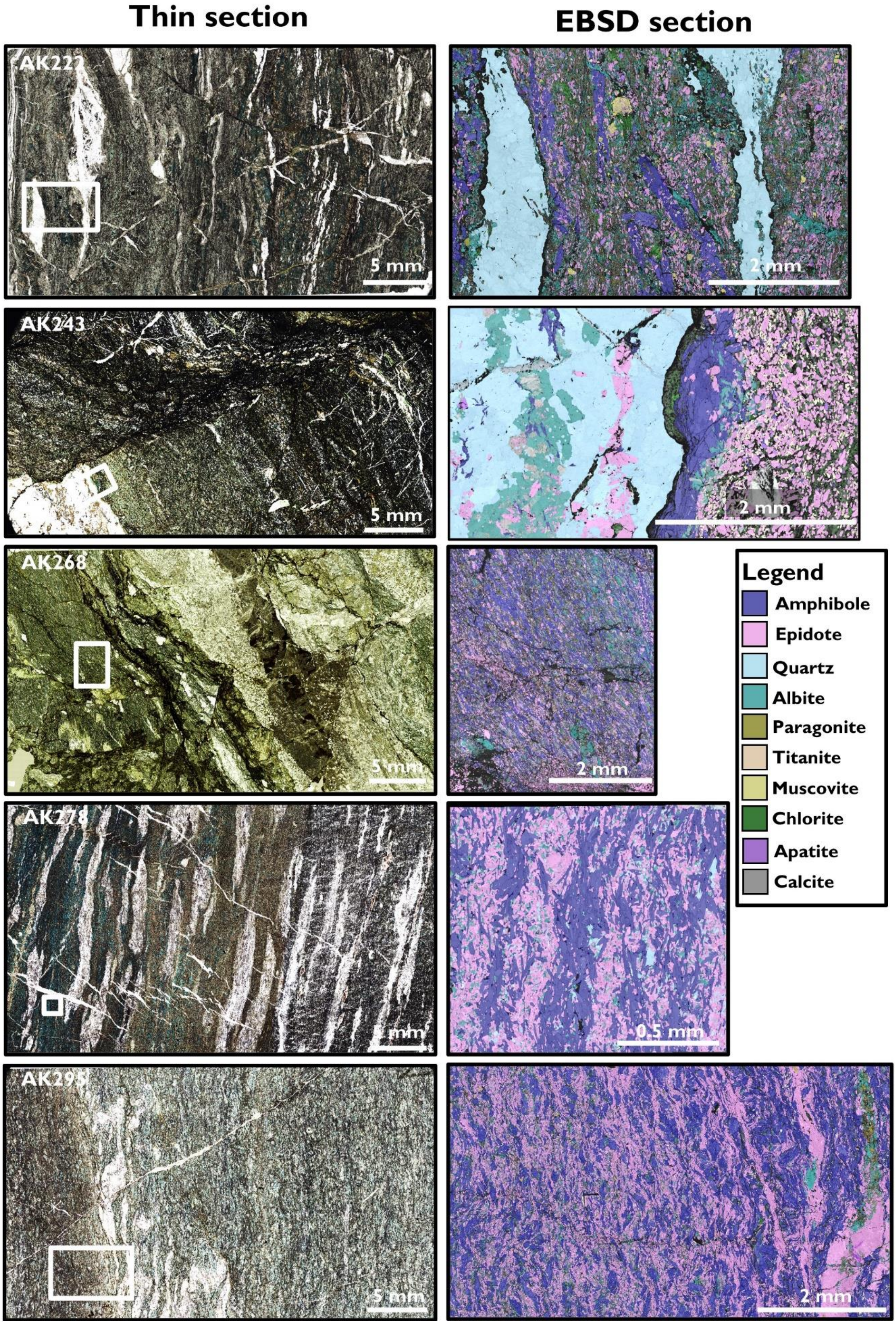

Figure S1 | Overview thin sections with EBSD locations in the white boxes, and phase maps of EBSD sections.

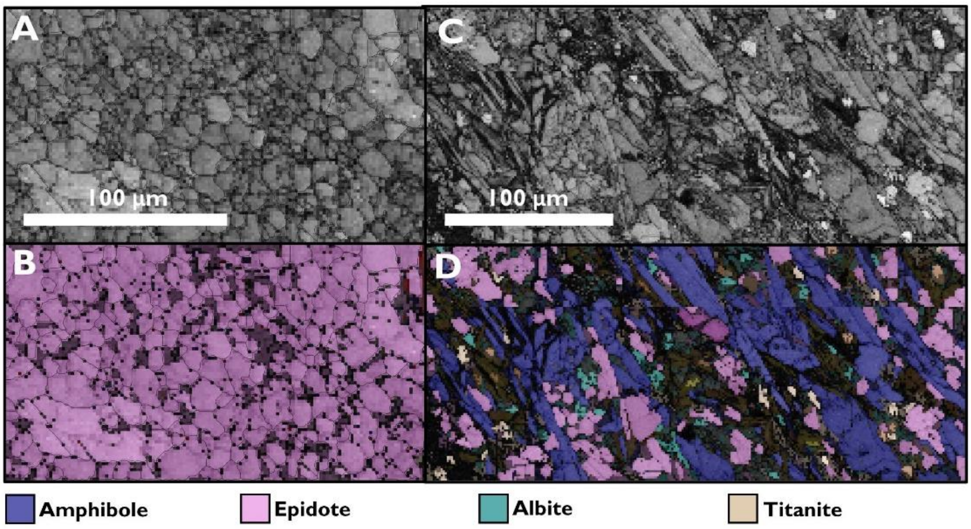

Figure S2 | Grain size measurements are done on grains with 8 or more pixels, in which the colored minerals are taken into account. A and B represent a fine-grained epidote compositional band, C and D a mixed amphibole-epidote-albite matrix.

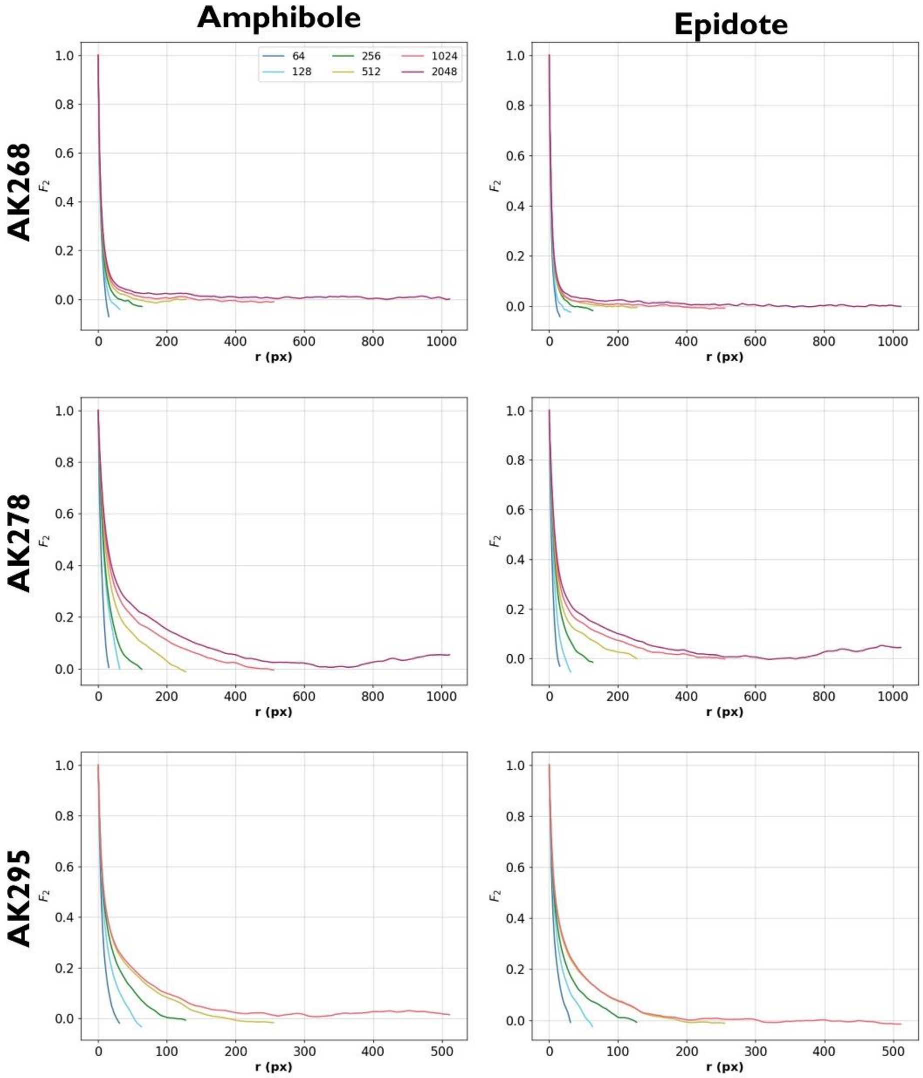

Figure S3 | Representative Elementary Size analysis on three samples for amphibole and epidote based on methodology of Amiri et al. (2023). For sample parts, see Fig. 8.

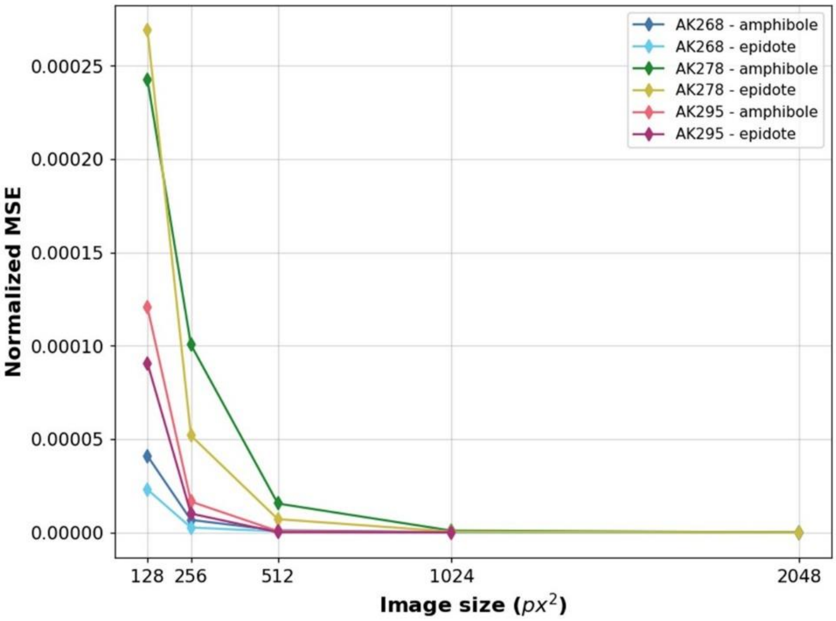

Figure S2 | Conclusion of Representative Elementary Size analysis on three samples for amphibole and epidote based on methodology of Amiri et al. (2023). For sample parts, see Fig. 8.

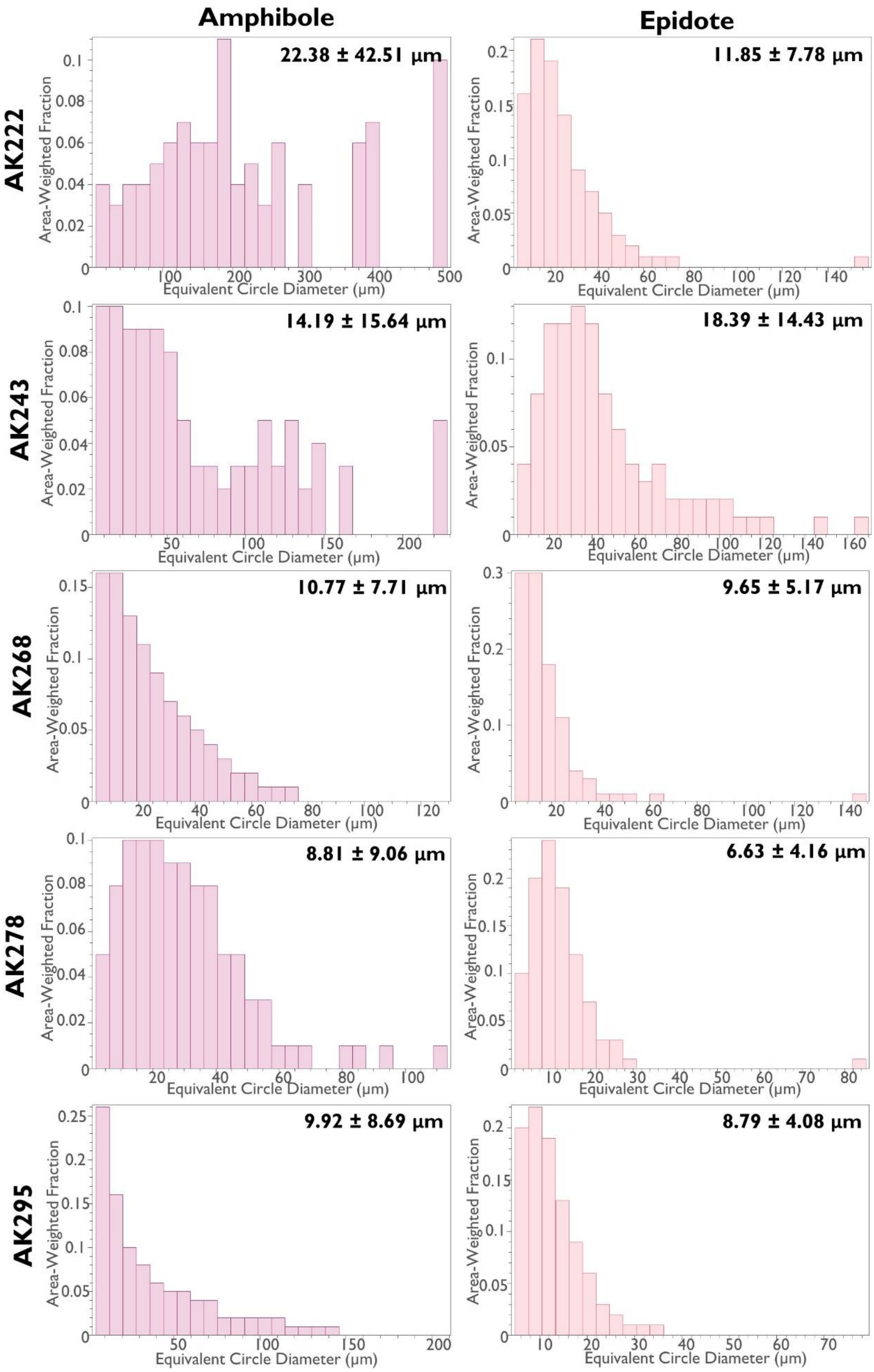

Figure S5 | Grain size distribution of amphiboles and epidotes, taken from Aztec Crystal.

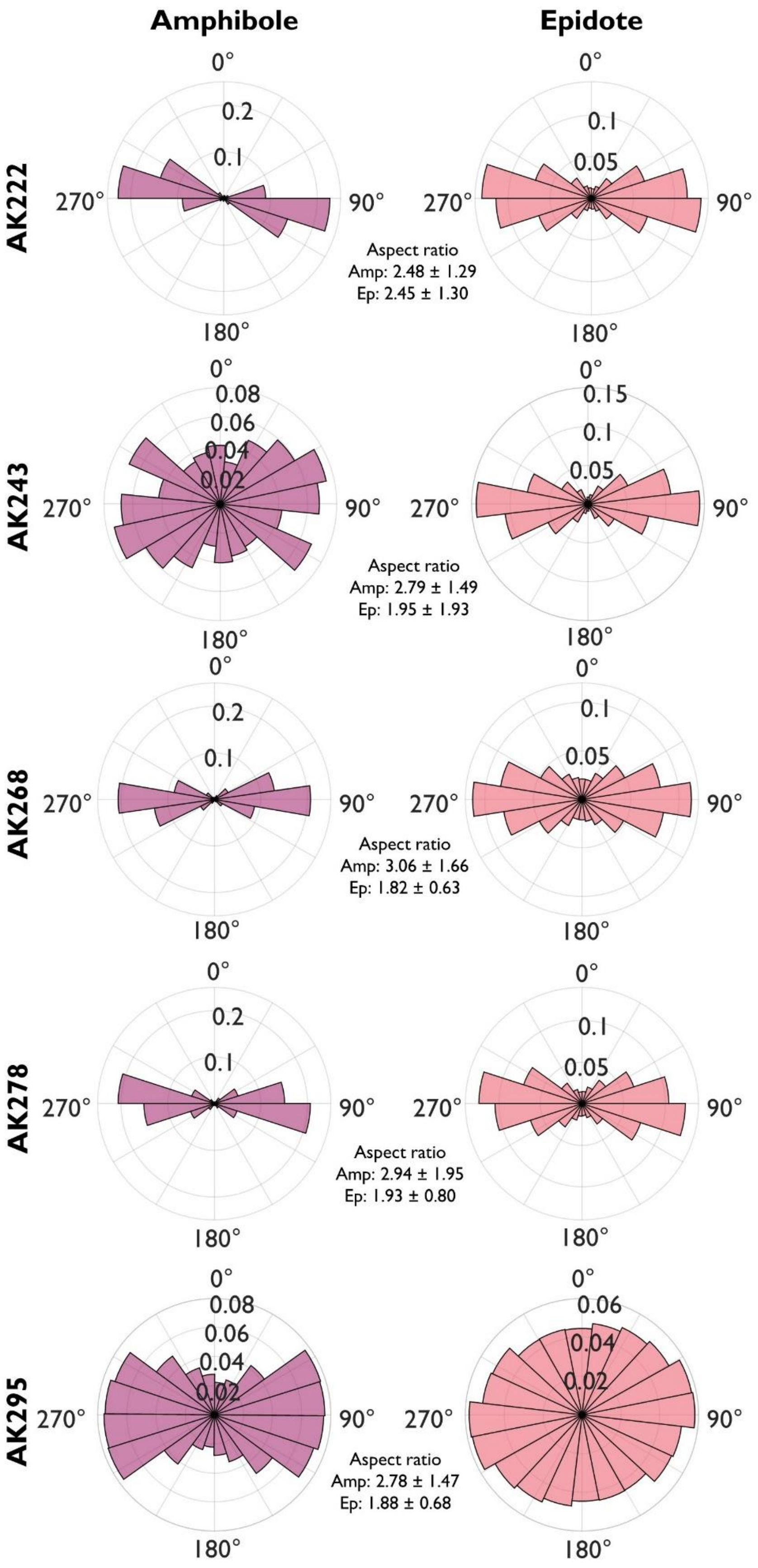

Figure S6 | Shape preferred orientations (SPOs) and aspect ratios of amphiboles and epidotes, calculated with MTex. The horizontal bar indicates the foliation.

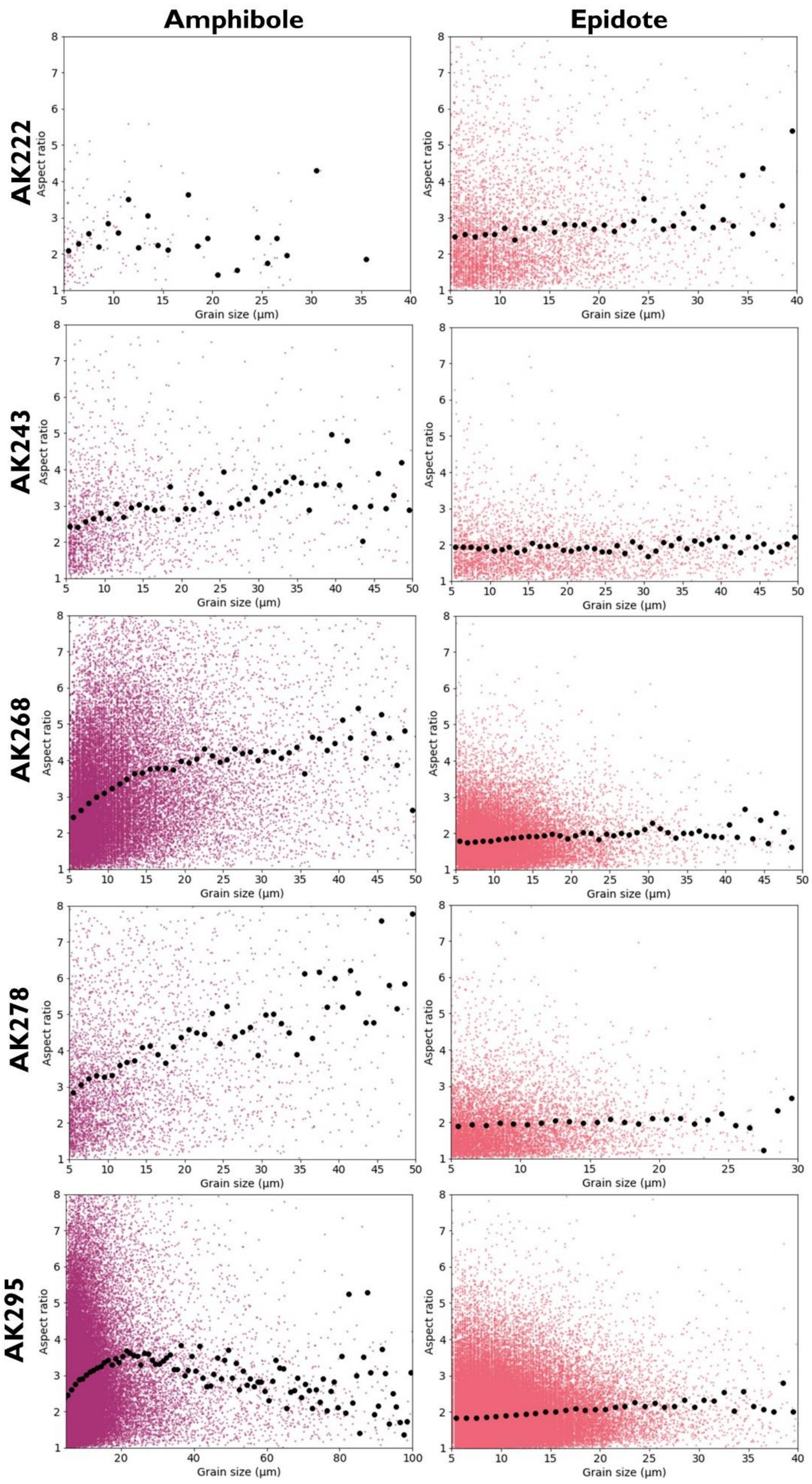

Figure S7 | Grain size vs aspect ratio, data taken from Aztec Crystal. Black dots represent mean values of every 1 µm.

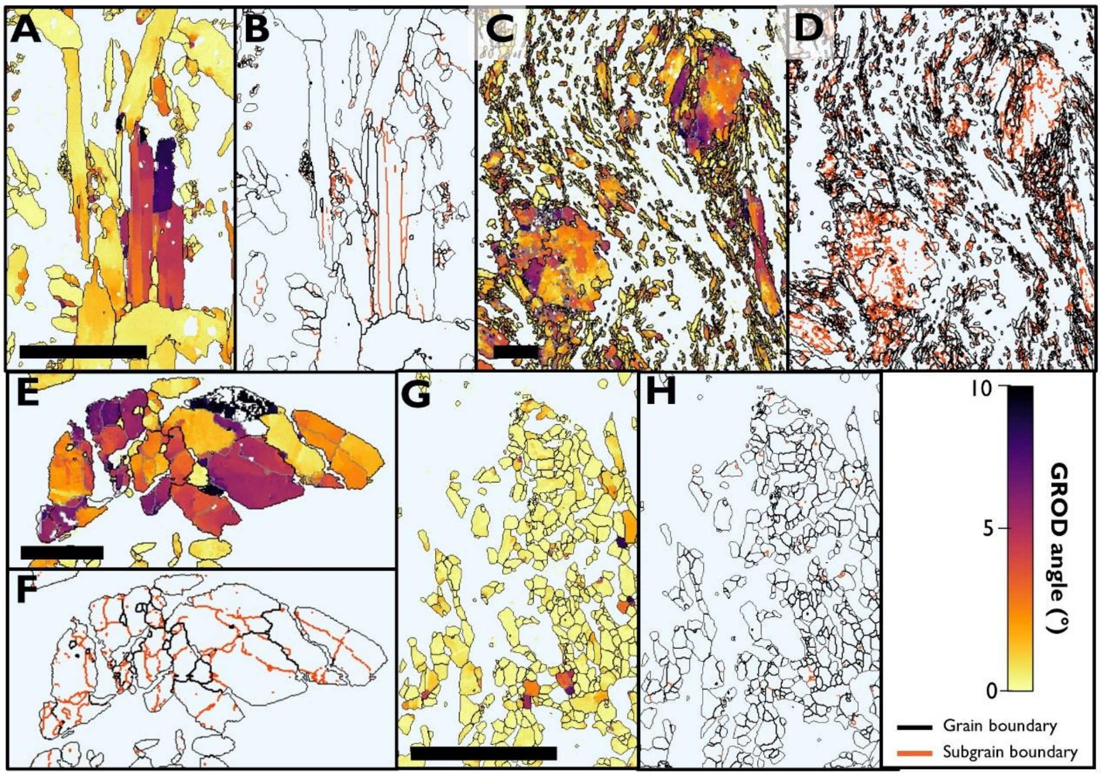

Figure S8 | Supplementary figures of GROD angles and grain and subgrain boundaries in amphiboles (A-D) and epidotes (E-H). Each scale bar represents 100 μm.

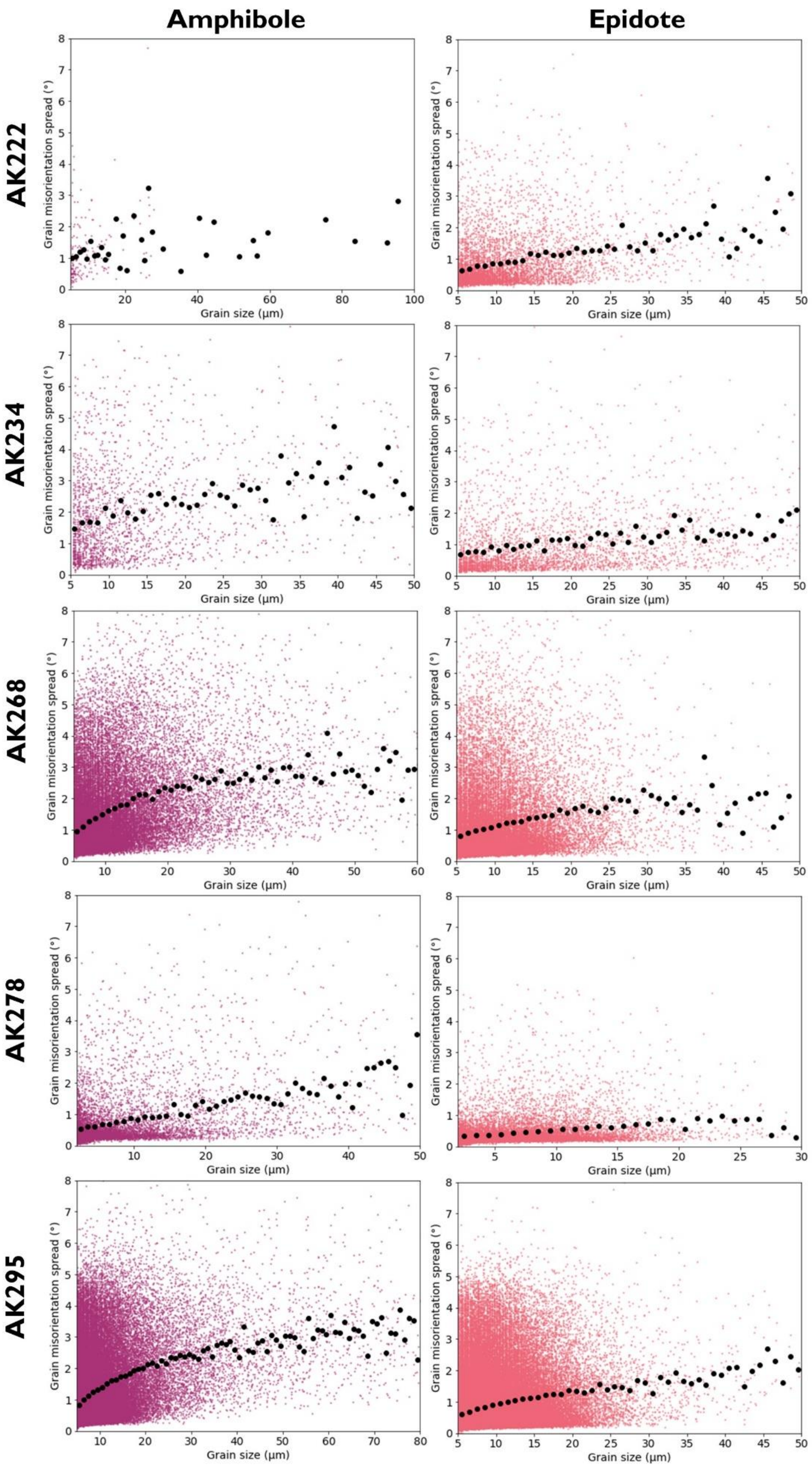

Figure S9 | Grain size vs grain misorientation spread, data taken from Aztec Crystal. Black dots represent mean values of every 1 µm.

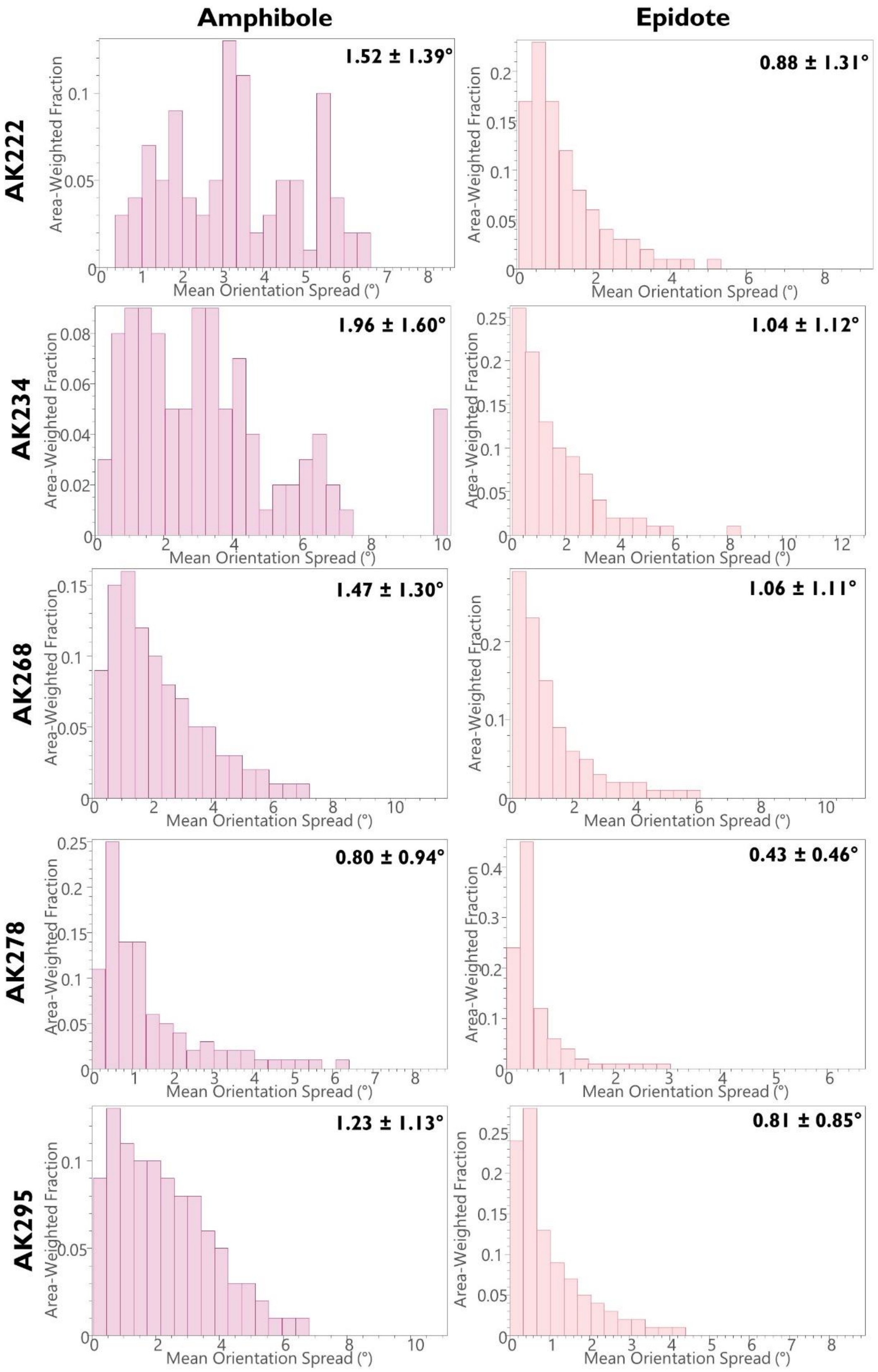

Figure S10 | Mean Orientation Spread of amphiboles and epidotes, taken from Aztec Crystal.

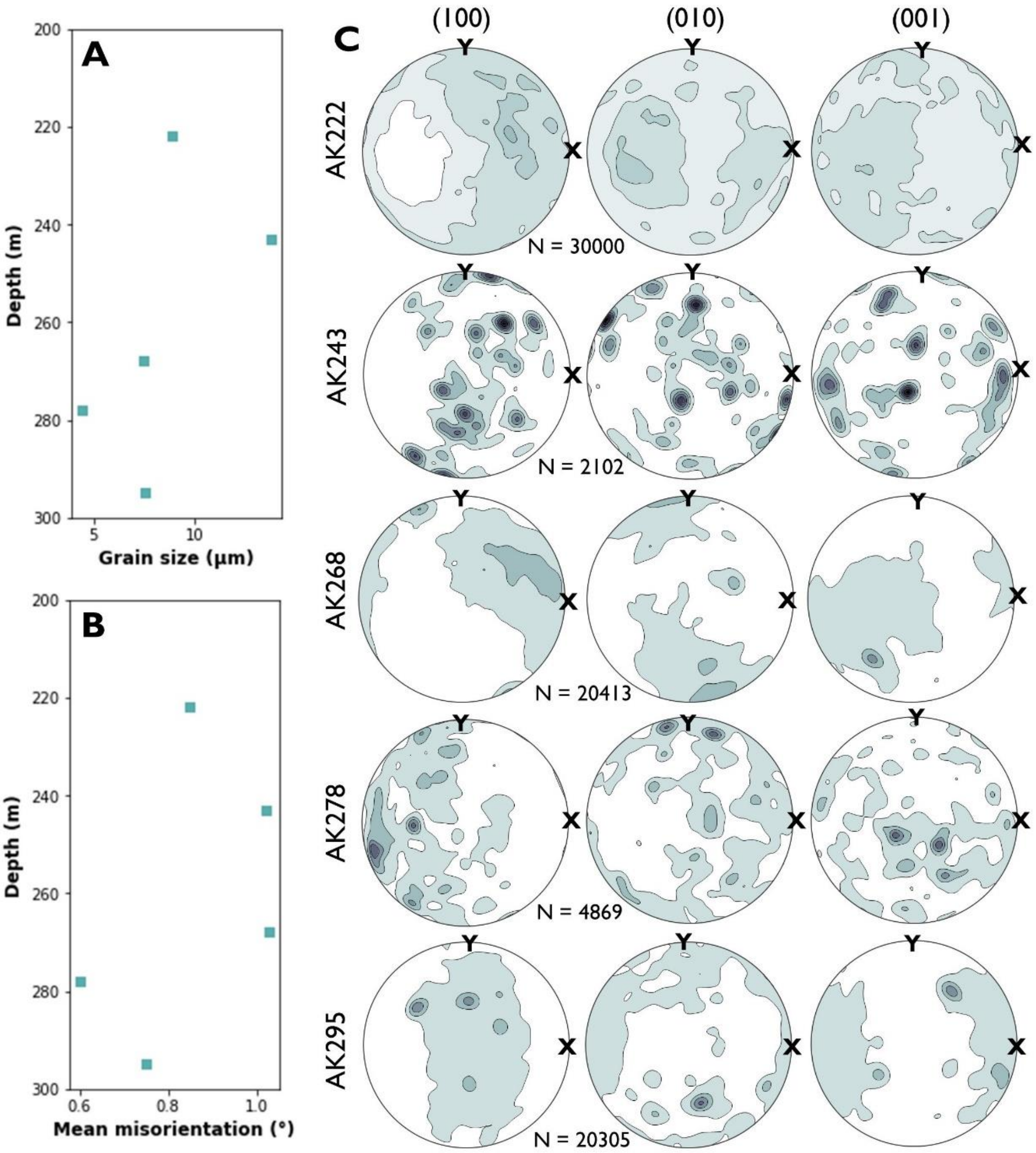

Figure S11 | (A) Mean grain size of albite for 5 EBSD sections. (B) Mean internal misorientation of albite for 5 EBSD sections. (C) CPO pole figures of albite for 5 EBSD sections.

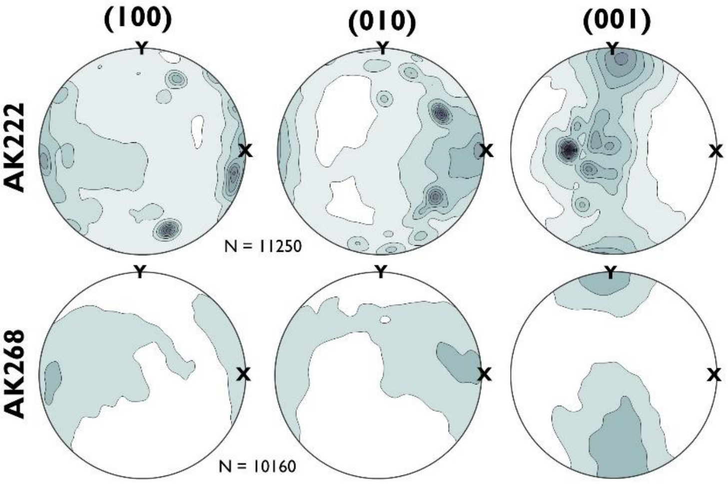

Figure S12 | CPO pole figures of muscovite from two EBSD sections.

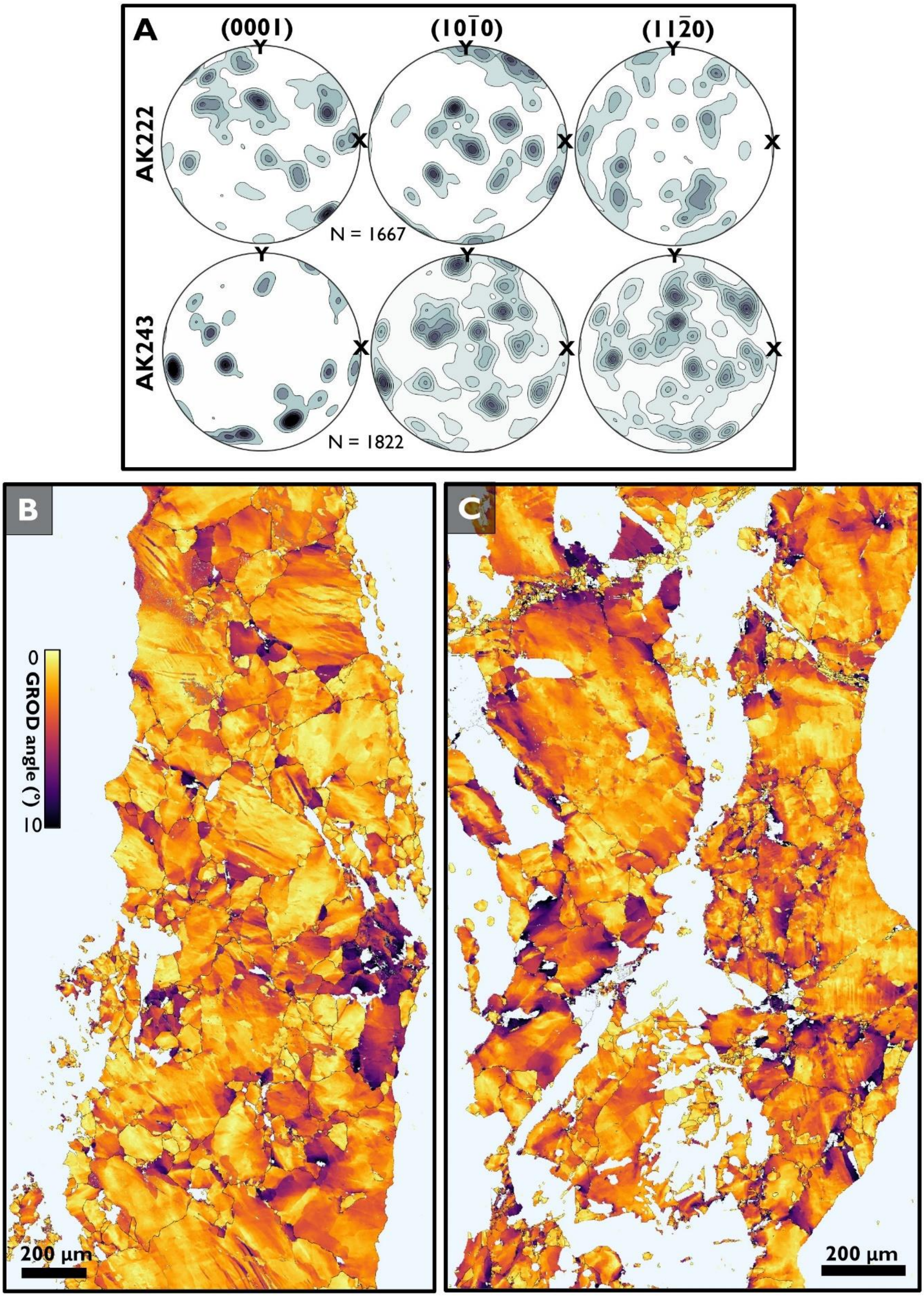

Figure S13 | (A) CPO pole figure of quartz from two EBSD sections, (B) GROD angle map of AK222, (C) GROD angle map of AK243.

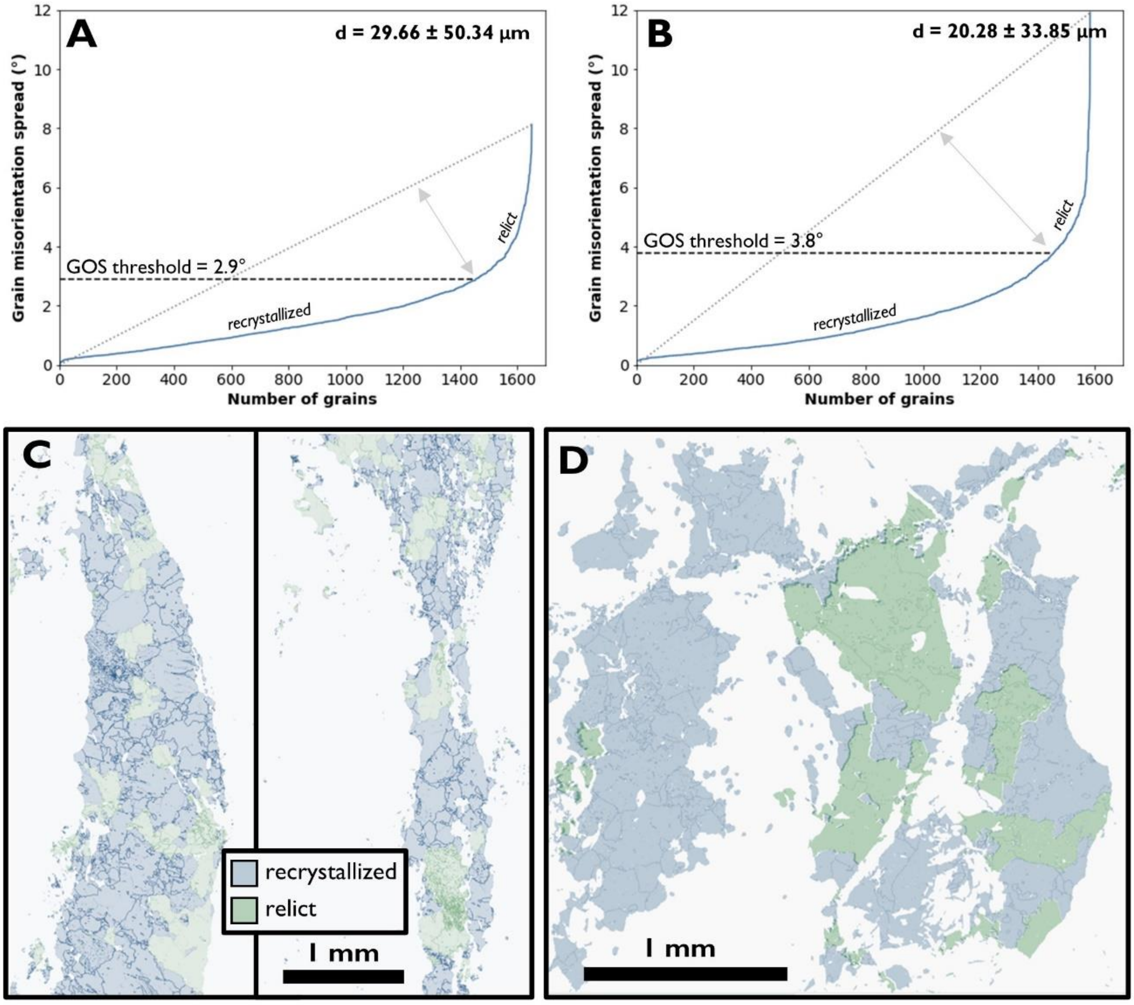

Figure S14 | Knee curve plots to determine the recrystallized grain size for sample AK222 (A) and AK243 (B). Maps showing recrystallized and relict grain sizes according to this method of Cross et al. (2017) for AK222 (C) and AK243 (D).